Check for updates

JGR Planets

RESEARCH ARTICLE
10.1029/2020JE006493

Special Section:
InSight at Mars

Effects of a Large Dust Storm in the Near-Surface Atmosphere as Measured by InSight in Elysium Planitia, Mars. Comparison With Contemporaneous Measurements by Mars Science Laboratory

D. Viúdez-Moreiras[1], C. E. Newman[2], F. Forget[3], M. Lemmon[4], D. Banfield[5], A. Spiga[3], A. Lepinette[1], J. A. Rodriguez-Manfredi[1], J. Gómez-Elvira[1], J. Pla-García[1], N. Muller[6], M. Grott[6], and the TWINS/InSight team

[1]Centro de Astrobiología (CSIC-INTA) and National Institute for Aerospace Technology (INTA), Madrid, Spain, [2]Aeolis Research, Pasadena, CA, USA, [3]Laboratoire de Météorologie Dynamique (LMD/IPSL), Sorbonne Université, Centre National de la Recherche Scientifique, EÉcole Polytechnique, EÉcole Normale Superieure, Paris, France, [4]Space Science Institute, College Station, TX, USA, [5]Cornell Center for Astrophysics and Planetary Science, Cornell University, Ithaca, NY, USA, [6]German Aerospace Center (DLR), Berlin, Germany

Key Points:
- InSight measured the atmospheric response to a large dust storm at L_s ~ 320° in MY34
- Diurnal pressure amplitudes abruptly increased and vortex pressure drop decreased after an initial increase during storm onset
- Storm onset strongly modified flows dominated by the Hadley circulation and local slopes to include the effect of enhanced tidal flows

Supporting Information:
- Supporting Information S1

Correspondence to:
D. Viúdez-Moreiras,
viudezmd@inta.es

Citation:
Viúdez-Moreiras, D., Newman, C. E., Forget, F., Lemmon, M., Banfield, D., Spiga, A., et al. (2020). Effects of a large dust storm in the near-surface atmosphere as measured by InSight in Elysium Planitia, Mars. Comparison with contemporaneous measurements by Mars Science Laboratory. *Journal of Geophysical Research: Planets*, *125*, e2020JE006493. https://doi.org/10.1029/2020JE006493

Received 22 APR 2020
Accepted 6 AUG 2020
Accepted article online 11 AUG 2020

©2020. The Authors.
This is an open access article under the terms of the Creative Commons Attribution License, which permits use, distribution and reproduction in any medium, provided the original work is properly cited.

Abstract NASA's InSight landed in Elysium Planitia (~4.5°N,136°E) at L_s ~ 296° (November 2018), right after the decay of the 2018 Global Dust Storm (GDS) and before the onset of the 2019 Large Dust Storm (LDS) at L_s ~ 320° (January 2019). InSight's cameras observed a rise in the atmospheric opacities during the storm from ~0.7 to ~1.9, similarly to contemporaneous measurements by Curiosity in Gale crater. Pressure tides were strongly affected at the locations of InSight and Curiosity. In particular, the diurnal pressure mode experienced an abrupt increase during the onset of the LDS, similar to that measured by Curiosity, most likely due to longitudinally asymmetric dust loading. Later, the dust was redistributed around the planet and the semidiurnal mode evolved according to dust opacity in both missions. Before and after the onset of the storm, the observed wind patterns resulted from the interaction between regional and local slope flows induced by topography, which all produced a diurnal perturbation superimposed on a mean flow, dominated by the Hadley cell but with modifications due to channeling effects from the regional topography. However, the onset of the LDS modified this to a scenario consistent with enhanced tidal flows. The local air temperatures are strongly perturbed by the lander's thermal effects, and their retrieval significantly depends on wind patterns, which changed during the course of the dust storm. Observations suggest a decrease in convective vortices during the dust storm; however, vortex activity remained strong during the storm's onset due to the increase in wind speeds.

Plain Language Summary NASA's InSight landed in Elysium Planitia, Mars, at November 2018, right after the decay of the 2018 Global Dust Storm and before the onset of the 2019 Large Dust Storm (LDS) (January 2019). InSight's cameras observed a rise in the atmospheric opacities during the storm from ~0.7 to ~1.9, similar to contemporaneous measurements by Curiosity in Gale crater. Pressure tides were strongly affected. In particular, the amplitude of the pressure harmonics with a period of 1 sol (diurnal pressure mode) experienced an abrupt increase during the onset of the LDS, similar to that measured by Curiosity, most likely as a result of different dust loading as a function of location. Later, the dust was redistributed around the planet and the semidiurnal pressure mode evolved according to dust opacity in both missions. The onset of the storm modified the wind patterns, probably due to enhanced tidal flows. The measured air temperatures were strongly perturbed by the lander's thermal effects. The daytime lander effects significantly depend on wind patterns. Observations suggest an impact on convective vortices, with an overall decrease during the LDS. However, the vortex activity remained strong during storm onset due to the increase in wind speeds.

1. Introduction

Local and regional dust storms are ubiquitous on Mars, particularly between the southern spring and autumn equinoxes, areocentric solar longitudes L_s ~ 180–360° (e.g., Cantor et al., 2001; Wang & Richardson, 2015; Zurek & Martin, 1993). Every few years, regional storms grow and merge, covering all longitudes over most of both hemispheres in events known as global dust storms (GDS), planet-encircling dust storms, or global dust events. Although significant modeling efforts have been performed (e.g., Basu et al., 2006; Rafkin, 2009), this phenomenon involves an interplay of mechanisms that remains, to date, little understood and hence unpredictable, in part due to both the rarity of such events and the sparse data acquired from orbit and the surface. Mars Year (MY) 34, lasting from mid-2017 to early 2019, was remarkable in this sense, given that it included both a GDS (lasting from L_s ~ 180° to 250°) (Guzewich et al., 2019; Lemmon et al., 2019) and a subsequent large dust storm (LDS) lasting from MY34, L_s ~ 320° to MY35, L_s ~ 20°. Both storms were monitored by several spacecraft in orbit around Mars (e.g., Montabone et al., 2020).

The entire MY34 GDS was monitored from the surface by the Mars Science Laboratory (MSL) rover inside Gale crater (~4.5°S, ~137.4°E), while the storm's onset was monitored by the Opportunity Mars Exploration Rover in Meridiani Planum (~0.2°N, 357.5°E). While MSL is powered by a radioisotope thermoelectric generator (RTG), the high dust opacities and thus greatly reduced solar irradiance at the surface resulted in the unfortunate loss of solar-powered Opportunity as the GDS approached its peak, receiving the last communication from the lander in June 2018. On MSL, the Rover Environmental Monitoring Station (REMS) instrument (Gómez-Elvira et al., 2012) provided extremely valuable meteorological data (Guzewich et al., 2019; Viúdez-Moreiras et al., 2019), complementing previous observations by the Viking Landers (e.g., Ryan & Henry, 1979; Ryan & Sharmann, 1981; Tillman, 1988; Zurek & Martin, 1993).

All atmospheric variables measured by MSL REMS were strongly affected by the MY34 GDS, although at different times. During storm onset, the diurnal maximum in the UV radiation decreased by 90% between Sols 2075 (MSL's Mast Camera optical depth ~1) and 2085 (optical depth ~8.5). The diurnal amplitude in air and ground temperatures were reduced by 56 and 35 K, respectively, along with a decrease in the daily mean of ~2 and ~4 K. Between MSL Sols 2085 and 2130, the usual stable inversion layer during nighttime was absent near the surface, as the ground presented higher temperatures than near-surface air masses (Viúdez-Moreiras et al., 2019). The daytime surface-to-air thermal gradient and, probably, wind speeds were strongly reduced, resulting in no rapid, short-lived pressure drops (associated with convective vortices) exceeding 0.5 Pa or dust devils being observed by MSL, between Sols 2083 and 2107 (Guzewich et al., 2019). The near-surface water vapor abundance, inferred from the relative humidity, pressure, and temperature measurements, suggested an overnight increase during the storm at MSL's general location in Gale crater and a decrease during the daytime, although with a high level of uncertainty due to MSL's sensor constraints (Viúdez-Moreiras et al., 2019). It was hypothesized in Viúdez-Moreiras et al. (2019) that the combined effect of a reduction in the strength of an adsorption and desorption mechanism in the regolith, which is likely driving the diurnal cycle in the near-surface water vapor abundance, and the enhanced vertical mixing suggested at night during the dust storm period could be driving the observed effect in the diurnal cycle considering that the inferred water vapor abundances during the GDS are correct. Savijärvi et al. (2020) attempted to simulate the MY34 GDS surface water abundance within Gale crater by means of a one-dimensional model and further assumptions, but simulations did not match the observations, and they proposed an additional source of water vapor to minimize the model mismatch. Additional and accurate surface measurements will contribute to discern the role of exchange with the regolith. Also, the semidiurnal and terdiurnal pressure mode amplitudes were strongly enhanced and peaked after the local opacity maximum measured by MSL's Mast Camera (Mastcam), suggesting deviations in the dust abundance in Gale crater regarding its neighborhood even during the decay of the storm (Viúdez-Moreiras et al., 2019). This was confirmed by ground-based observations (Sánchez-Lavega et al., 2019) and by orbital observations made by the Thermal Emission Imaging System onboard Mars Odyssey (Smith, 2019) and by Mars Climate Sounder (MCS) onboard Mars Reconnaissance Orbiter (MRO) (e.g., Kass et al., 2019; Montabone et al., 2020). This differs from the strong correlation between tidal amplitudes and local opacity observations obtained in a nominal atmospheric scenario, which suggest that the optical depths measured at Gale crater are usually roughly representative of the global mean. The difference is explained by the GDS producing more intense dust lifting in certain locations, thus producing strong inhomogeneities in the atmospheric dust content.

Although measuring the near-surface wind patterns could have added valuable information for properly characterizing the effects of the GDS at Gale crater, the REMS wind sensor (WS) was not available after late 2016, following further damage to sensor boards that occurred during the second Bagnold Dunes campaign, in addition to that which occurred during MSL's landing (Newman et al., 2017; Viúdez-Moreiras et al., 2019a, 2019b).

The solar-powered InSight lander arrived in Elysium Planitia (~4.5°N, 136°E), within ~600 km of MSL, shortly after the decay of the MY34 GDS in November 2018 (at L_s ~ 296°, after northern winter solstice). This fortuitous timing avoided the risks to a solar-powered lander of a GDS yet still enabled InSight to monitor the onset, growth, and decay of the MY34 northern winter LDS, as felt in Elysium Planitia. Here, we present the effects of the MY34 LDS on the near-surface atmosphere as measured by InSight, including dust opacity, atmospheric pressure, air and ground brightness temperatures, and wind speed and direction. This is the first time since the Viking missions in the 1970s that a spacecraft with a fully functional WS has measured the effect of a regional dust storm. In parallel, MSL observed the effects of the LDS inside Gale crater, a few hundred kilometers to the south, and therefore, we also compare the InSight observations with contemporaneous measurements by MSL, particularly dust opacity and atmospheric pressure (see section 4).

This article is structured as follows: Section 2 describes the sensors used in this work and presents several issues related to the interpretation of measurements. Section 3 describes the Elysium Planitia atmospheric context during northern winter and presents the effects of the LDS on the diurnally averaged meteorology. Section 4 focuses on the diurnal cycles observed by InSight during the event and their comparison to diurnal cycles before and after the LDS and at MSL's location. Section 5 focuses on convective vortex activity and its variation during the storm. Finally, section 6 presents the article's summary and conclusions.

2. The InSight Mission and the APSS and HP^3 Instruments

InSight carries, among other instruments, the Auxiliary Payload Sensor Suite (APSS), which includes a pressure sensor and the Temperature and Winds Sensor (TWINS) package (Banfield et al., 2019), inherited from the previous sensors sent to Mars as part of MSL REMS (Gómez-Elvira et al., 2012). Also, a radiometer (RAD) used to measure the temperature of the surface is included in the Heat Flow and Physical Properties Package (HP^3) (Spohn et al., 2018). These instruments allow near-surface wind patterns, pressure, and air and ground temperatures to be measured at InSight's landing site and—given its proximity to MSL's location in Gale crater—complement observations being performed by MSL. The latter is of particular interest given the damage the REMS WS suffered during MSL's landing, resulting in low reliability for most of the wind data available for the northern winter season in particular (Viúdez-Moreiras et al., 2019a, 2019b), which prevents a full understanding of the diurnal and seasonal wind patterns in Gale crater and especially of the interaction between local, regional, and large-scale circulations. Comparisons of the InSight data with data acquired at the MSL site help to interpret how the large-scale, regional, and local circulations interact to produce the diurnal cycle of winds observed at each site and to improve general circulation model (GCM) predictions for both regions.

The APSS sensors measure continuously, with a sampling frequency of 1 Hz in the case of the WS and air temperature sensor (ATS) and 20 Hz for the pressure sensor. However, due to data transmission constraints, only a subset of the full data set was downlinked to Earth near the beginning of the mission (10 Hz for pressure and 0.1 Hz for winds and temperatures), including the period containing the LDS. The exceptions were during "event requests"—periods determined to be of particular interest for seismology, weather, and so forth based on examination of the lower-resolution data—for which higher-frequency data were downlinked.

2.1. Opacity Measurements

Optical depth measurements are routinely performed by InSight via sky imaging. As the InSight cameras cannot image the Sun, they cannot be used to directly determine solar extinction as for other Mars missions (Lemmon et al., 2015, 2019). Instead, the cameras are used to image the southern sky. Early in the mission, the Instrument Deployment Camera (IDC) was used, while later, the Instrument Context Camera (ICC) was used, and the IDC was not available due to operational reasons. After a validation period in the first

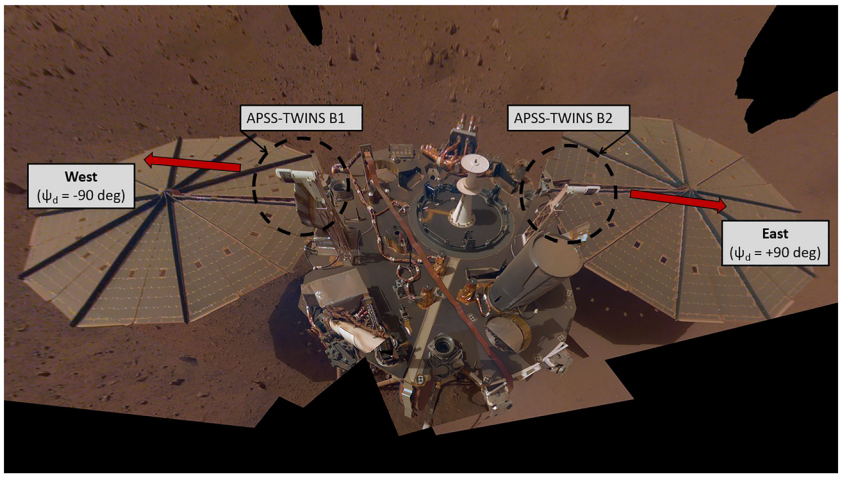


Figure 1. InSight platform, highlighting the APSS-TWINS booms (APSS-TWINS B1 and B2) and the wind direction Ψ_d reference system used in this work ($-180° < \Psi_d \leq 180°$, with the origin pointing to the north). Credits: NASA/JPL-Caltech.

4 months of the mission, ICC was certified for use and has become the dominant instrument for opacity measurements.

The cameras and the opacity pipeline are discussed in Maki et al. (2018), while the rationale and the methodology for the measurements are discussed in Spiga et al. (2018). In brief, a radiative transfer model is used to determine opacity above the lander at an effective wavelength of ~600 nm (Maki et al., 2018) from the sky images. Due to the expectation and reality of variable dust contamination on the optics, the retrieval focuses on the sky gradient with elevation at constant scattering angle rather than absolute photometry. The sky radiance was modeled based on input dust single scattering properties and the scattering geometry of each image. DISORT, a discrete-ordinates radiative transfer code (Stamnes et al., 1988), was used for the forward model. Opacity is varied to minimize a chi-squared fit to the gradient d (log(I))/dφ, where I is intensity and φ elevation angle. Measurements are obtained either in the afternoon or during the morning, with variable acquisition frequency (Figure 1) depending on the surface operations schedule. The most common times for observations are with solar elevation angles between 20° and 25°, therefore about 16:20–16:40 Local True Solar Time (LTST) and 7:20–7:40 LTST. The measurement uncertainty is ~0.1 (1σ) for both cameras (IDC ad ICC), except in the first sols of mission, when the uncertainty was sometimes higher (Figure 1).

2.2. Atmospheric Pressure Measurements

The pressure sensor consists of a pressure transducer and a set of tubing to connect the sensor to the inlet, which is designed to minimize the effect of dynamic pressures on the pressure measurement (Banfield et al., 2019). The observational noise is ~10^{-2} Pa, and the sampling rate can be as high as 20 Hz (although the response time constraint is ~7 Hz), significantly greater than previous sensors on Mars. We use 10 min average measurements for this study, except for the vortex part of the study, in which high-frequency data are needed.

2.3. Wind Measurements

The TWINS WS (Banfield et al., 2019) uses thermal anemometry to record winds such as the Viking Landers' WS (Chamberlain et al., 1976; Hess et al., 1977; Jones et al., 1979) and MSL REMS designs (Domínguez et al., 2008; Gómez-Elvira et al., 2012). However, unlike the wire sensors used by Vikings, the REMS and TWINS WS instead use thin titanium film resistors patterned on the surface of a silicon chip (Domínguez et al., 2008). The TWINS WS consists of two booms (B1 and B2) angled at 180° to each other and mounted on the lander deck, as shown in Figure 1. They are located 26.5 cm from the deck, which is ~90 cm above the ground (InSight lander has a small tilt that puts the APPS-TWINS B1 a few cm higher than B2, relative to the ground). A retrieval algorithm examines data from both booms and compares them with data acquired during wind tunnel calibration experiments, in order to determine the ambient wind speed and direction at

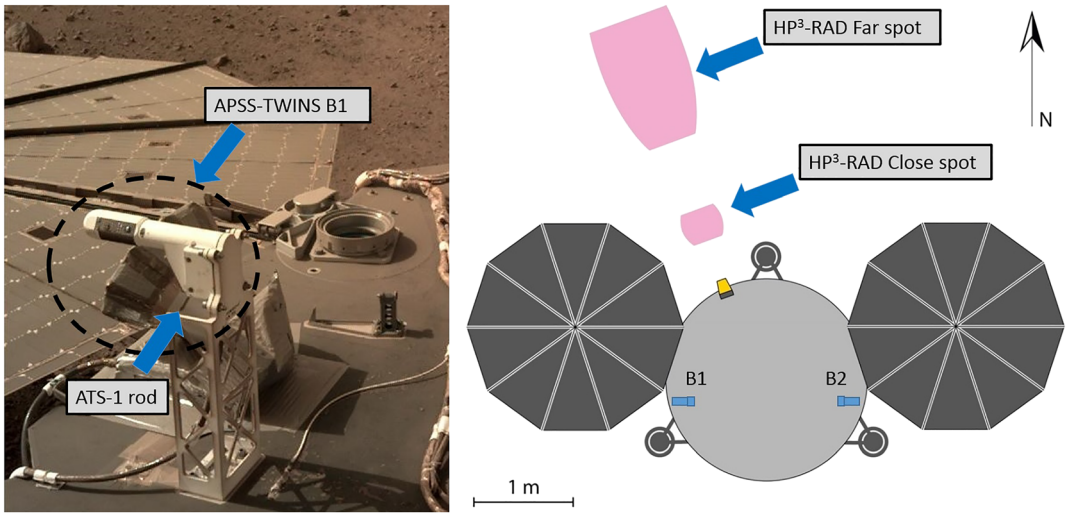


Figure 2. (left) APSS-TWINS B1 boom layout, showing the ATS rod. TWINS B2 presents a similar layout. Credits: NASA/JPL-Caltech. (right) HP^3-RAD close spot and a far spot, relative to the lander location. Adapted from Spohn et al. (2018).

1 Hz of sampling frequency (Gómez-Elvira et al., 2012). The TWINS WS is composed of the flight spares from the REMS WS, with improved electronics and calibration procedures. The REMS WS suffered damage during MSL's landing in 2012, making one of the two booms inoperative, and became inoperable altogether in late 2016 due to the failure of the remaining boom (Viúdez-Moreiras et al., 2019a, 2019b). Although the main REMS WS problems—caused by sensor damage during MSL's landing and noisy electronics (Newman et al., 2017; Viúdez-Moreiras et al., 2019a)—are fortunately not involved in the InSight measurements, a concern for both missions is whether the *observed* winds represent the *ambient* at the landing site. Wind measurements acquired by the WS represent the local wind field at each boom location and not the far field, because the lander/rover may slightly modify the wind speed and direction measured by the sensor. CFD simulations predict that the lander perturbation to InSight WS measurements is less than 20% in wind speed and 22.5° in wind direction for mean atmospheric conditions, supporting the accuracy of the observations. In addition, some elements on the deck can block the wind flowing from certain directions to produce blind areas. Also, the wind retrieval has problems identifying wind speed and direction for wind speeds less than ~2 m/s for reference pressure and temperatures at InSight's landing site (Banfield et al., 2020).

2.4. Air Temperature Measurements

The TWINS ATS consists of two independent sets of RTD thermistors (Pt1000 Class A), with each set located on a TWINS boom (Banfield et al., 2019; Gómez-Elvira et al., 2012). Each set is composed of three Pt1000s located at different positions within a 35 mm thin fin installed along the boom's vertical plane that contains the boom's longitudinal axis and with an angle of ~45° with respect to it (Banfield et al., 2019; Gómez-Elvira et al., 2012; Figure 2) (for simplicity, the set composed by the ATS rod and the boom is hereafter referred to as a boom as a whole). In order to take into account thermal contamination through the rod by conduction or solar radiation, a temperature retrieval is used to estimate the local temperature for both booms (T_{local1} and T_{local2}), decoupling these effects similarly to the REMS ATS retrieval (Gómez-Elvira et al., 2012; Mueller & Abu-Mulaweh, 2006). However, retrieved air temperatures in the vicinity of each boom are not necessarily the *ambient* air temperature, that is, the temperature far away from the lander, T^r_{air}, given that the fluid, and hence T_{local1} and T_{local2}, can be strongly affected by the lander's thermal contamination. In fact, T_{local1} and T_{local2} are found to be strongly affected by the wind patterns (section 4.2). Also, whereas the ATS on MSL are generally overheated during the whole sol due to solar radiative heating and MSL's RTG, InSight's ATS are overheated during the day by solar radiative heating and overcooled during the night due to the strong radiative cooling of the nearby solar panels. Although the overheating (~15–20 K) can be much stronger than the overcooling (~10 K), both are major problems for interpreting the raw measurements.

Here, we use a simple algorithm, inherited from REMS (Gómez-Elvira et al., 2012; Mueller & Abu-Mulaweh, 2006), to provide a rough estimation, T_{air}, of the air temperature, T^{r}_{air}, where $T_{air} = \min\{T_{local1}, T_{local2}\}$ (Temperature Estimation A). The effect of lander thermal overheating and instrumentation issues is thus strongly mitigated by picking up the minimum temperature between both retrievals T_{local1} and T_{local2}, as will be shown in section 4. However, nighttime thermal effects are not removed by this estimation, and considering the estimated T_{air} using the aforementioned equation derived from REMS can induce an additional ~2 K bias in the minimum temperatures reached during the nighttime than if we were using the $\max\{T_{local1}, T_{local2}\}$ relationship during nighttime, which is more appropriate given the nighttime platform overcooling. Thus, we include a better proxy for the nighttime temperatures, $T_{night} = \max\{T_{tip1}, T_{tip2}\}$ (Temperature Estimation B) where T_{tip1} and T_{tip2} are the temperatures located at the end of the thin fin installed along the ATS rod. Note that we use in this case T_{tip} instead of T_{local} because the ATS retrieval (Gómez-Elvira et al., 2012; Mueller & Abu-Mulaweh, 2006) performance decays under the low convection scenario involved during the nighttime. Also, we compute the daily mean air temperatures using the best guess of the air temperatures T^{p}_{air}, that is, T_{air} during the day until sunset and T_{night} since the sunset until dawn. Both estimates are presented for comparison. Heat transfer modeling would be required to better approach the true air temperature, that is, the ambient temperature without any perturbations, but is beyond the scope of this work.

2.5. Ground Brightness Temperature Measurements

We describe the effects of the LDS on the ground brightness temperature measured by the RAD within HP^3. The data from the RAD was downloaded during the first sols of mission in hourly intervals due to InSight data transmission constraints, but higher-frequency measurements are also possible and enabled in particular time periods. Two different regions or spots are sampled: a close spot and a far spot, relative to the lander location (Spohn et al., 2018; Figure 2). The areas of the footprints, defined by the full width at half maximum of sensitivity in the geometric calibration (Mueller et al., 2020), are 0.1 m^2 for the close spot and 0.9 m^2 for the far spot. For each one, a set of sensors measures the brightness temperatures in three spectral bands (8–14, 8–10, and 16–19 μm). We use here the measurements from the far spot (Figure 2), because it is less perturbed by lander thermal contamination or by shadowing during the day. Also, given that the last two spectral bands have comparatively large calibration uncertainties (Mueller et al., 2020), ground surface brightness temperature was retrieved based on the 8–14 μm channel only. The reflectance of the observed ground in the spectral bands of the HP^3-RAD is expected to be small because the emissivity is close to unity. A surface emissivity of 0.98 (Morgan et al., 2018; Mueller et al., 2020) is assumed in the computation of the surface ground temperature (hereafter referred to as ground temperature).

3. Evolution of Northern Winter and Spring Seasons and the MY34 2019 LDS at Elysium Planitia

3.1. The 2019 MY34 LDS as Observed From Orbit

In accordance to the expected behavior during the dust storm season (L_s ~ 180–360°), local dust events were observed from orbit during December 2018 (L_s ~ 300–310°) (Malin et al., 2018a, 2018b), including a slight increase in dust-lifting activity in last weeks of December (L_s ~ 310°). Significant local dust storms over Acidalia Planitia moved southward toward eastern Valles Marineris, while the plains of Amazonis, Arcadia, and Utopia developed repeated local dust storms (Malin et al., 2018b). Storm activity remained active for the northern hemisphere in last week of December (Malin et al., 2018c). Dust lifting along Acidalia Planitia, which started 1 week prior, continued south into Aonia Terra. During that time (L_s ~ 312°), a subsequent dust storm was initiated over Chryse Planitia (~30°N, 45°W) and moved southward toward Margaritifer Terra (~5°S, 30°W). Dust-lifting events were sparser for the southern hemisphere during that period (Malin et al., 2018c).

MRO-MCS data showed increased dust column abundance in longitudes ~30–70°W within the tropical region at L_s ~ 312° (Montabone et al., 2020; Figure 3), which grow to cover Chryse Planitia, Lunae Planum, Xanthe Terra, and Valles Marineris at L_s ~ 320° (Figure 3b). In the second week of January 2019 (L_s ~ 322°), the opacity rose significantly between 140°W and 50°E (Figure 3c) in the southern hemisphere as far as midlatitudes and from 70°W to 140°E in the northern hemisphere, reaching the MSL and InSight longitudes but with the bulk of atmospheric dust in northern latitudes. There were signs of strong

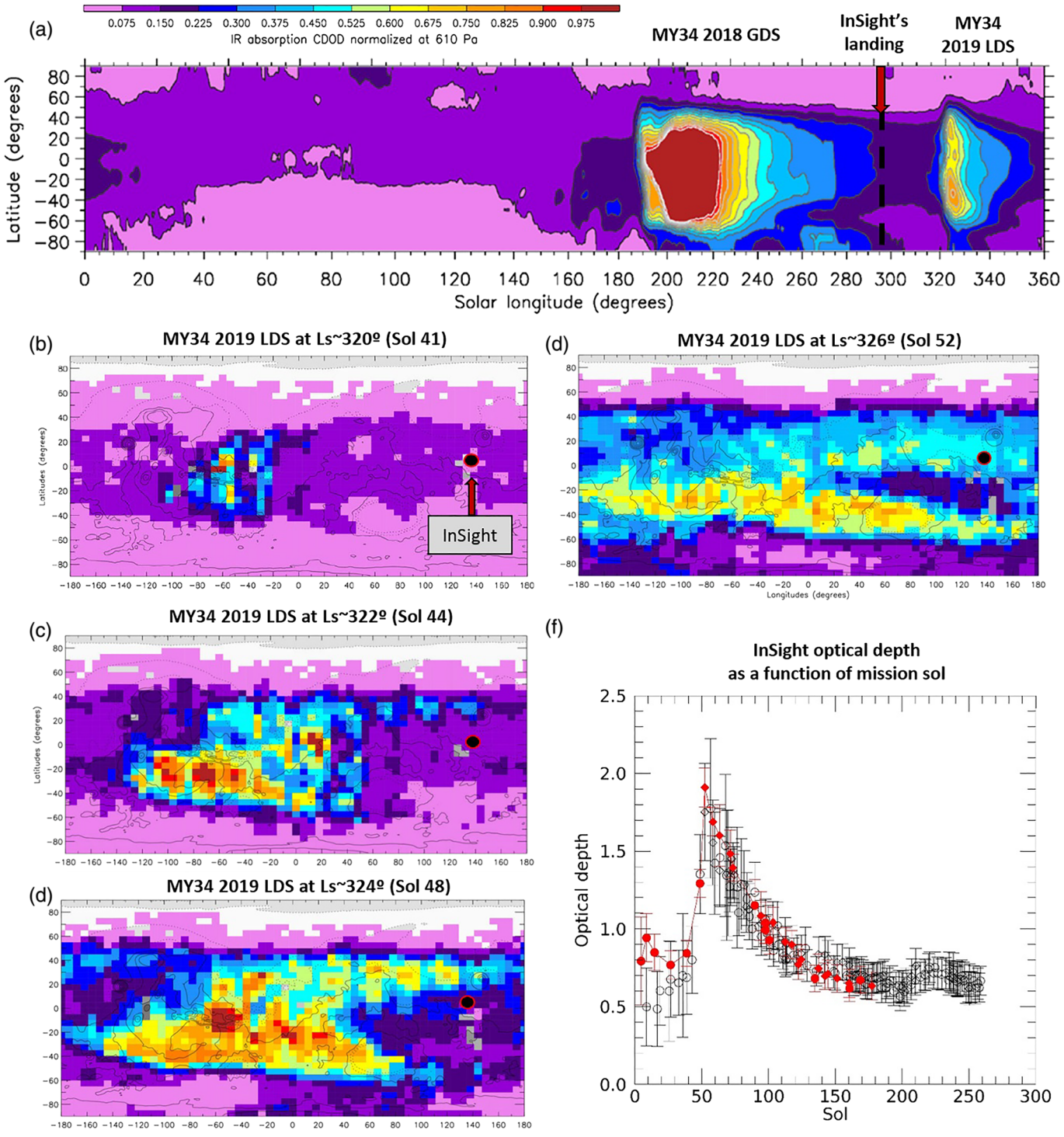


Figure 3. (b–e) Maps of daily average column dust optical depth at 9.3 μm normalized to 610 Pa, generated using interpolation from MCS observations by Montabone et al. (2020). Daily maps, demonstrating the evolution of the MY34 LDS, are shown for (b) L_s ~ 320°, (c) L_s ~ 322°, (d) L_s ~ 324°, and (e) L_s ~ 326°. InSight's general location is shown by a black dot. (a) shows the zonal-average of these daily maps as a function of L_s for MY34. InSight's landing time (L_s ~ 296°) after the MY34 GDS decay is highlighted as the black dashed line. (f) InSight's atmospheric optical depth, τ, at an effective wavelength of ~600 nm as measured by the IDC (red) and ICC (black) is shown as a function of InSight's mission sol, including error bars. Morning and afternoon observations are shown as diamonds and circles, respectively. A conversion factor of 3.2 can be used to convert the 9.3 μm absorption column optical depths to the visible ones (Montabone et al., 2020) at InSight's landing site.

temperature increase from MRO-MCS data, with a rapid growth in the lower atmosphere above the boundary layer in the southern midlatitudes centered on 50°S 55°W (David Kass, personal communication, 2019). The LDS continued to grow in the third week of January 2019 (L_s ~ 324°) and covered almost all longitudes with a strong asymmetric hemispheric response (Figure 3d), with further expansion peaking at L_s ~ 326° (Figure 3e). The LDS started its decay phase, and the most appreciable storm perturbations in the lower and middle atmosphere finished in the last week of January (L_s ~ 332°) (David Kass, personal communication, 2019), that is, roughly a month after the first effects were observed. Elevated levels of atmospheric dust, as a result of the abated LDS, persevered over most of Mars until the second half of March 2019, corresponding to the end of MY34 (Malin et al., 2019; Figures 3a and 3f). According to the classification described in Zurek and Martin (1993) and extended in Cantor et al. (2001), this storm can be classified as a late-winter *regional* storm (surface area $>1.6 \times l0^6$ km^2 and lasted more than 2 Sols), although its effects were much more intense than a typical regional dust storm (Cantor et al., 2001).

3.2. Northern Winter Season and Near-Surface Effects of the LDS as Observed by InSight in Elysium Planitia

InSight landed in Elysium Planitia (~4.5°N, 136°E) at L_s ~ 296° (Figures 3 and S1 in the supporting information), after the northern winter solstice and after the decay of the MY34 GDS. The first effects of the LDS, which originated on the other side of Mars, were observed in pressure and wind patterns by the InSight mission at L_s ~ 320°, corresponding to Sol 41 of the InSight mission; note that in this work "sols" always refer to InSight mission sols rather than sols of the MY. As described in section 3.1, the storm grew and released dust around the planet within only a few sols (Figures 3c–3e; L_s ~ 322–326°). InSight's cameras observed an increase in opacity (τ) at an effective wavelength of ~600 nm (section 2) from an average of ~0.7 to ~1.9 in that period (Figure 3f). Considering the IDC camera, opacity rose from 0.843 ± 0.084 in Sol 38 (L_s ~ 318°) to 1.910 ± 0.125 in Sol 52 (L_s ~ 326°) (Figure 3f). After that, the LDS decayed, and τ returned to seasonal values by Sol ~150. Contemporaneous measurements from MSL's cameras, which measure τ at a wavelength of 880 nm, showed a similar increase in Gale crater, with τ reaching ~1.8. Such high opacities were only previously observed during the MY34 GDS by MSL (in that case it reached ~8.5, remaining ~50 Sols above $\tau = 3$) and were not observed prior to this by InSight.

The trends in winds, temperature, and pressure acquired for these seasons (northern winter and early spring) showed a complex evolution due to the interaction between the nominal seasonal evolution and the LDS, whose effects began at Sol 41 and persisted as late as Sol ~150, when the dust opacity returned to seasonal values (Figure 3a). It is difficult to differentiate between the effects of the LDS and the nominal seasonal trend without having any observational reference for previous MYs; however, data acquired just before and after the storm and by other surface missions at nearby locations, in addition to modeling, can assist with the interpretation.

Figure 4 presents the daily mean, maximum, and minimum for pressure, air and ground temperatures, and wind speeds and directions, for the first sols of the mission encompassing the LDS period. Pressure, which is acquired at an altitude with respect to the MOLA geoid of −2,662 m, showed a decreasing trend since landing until Sol ~80 (L_s ~ 342°), from ~745 to ~720 Pa. This is in accordance with its expected behavior due to the increased deposition of CO_2 on the northern polar cap and contemporaneous REMS data acquired at Gale crater (not shown). Around Sol ~80, the daily mean pressure reached a minimum and then increased instead, due to net sublimation of CO_2 from Mars' polar caps, as observed at roughly the same point in the seasonal cycle by previous missions (e.g., Martínez et al., 2017), with slight differences in the L_s of the minimum depending mostly on latitude. Baroclinic waves were also observed to produce sol-to-sol variations, not only in pressure but also in other atmospheric variables such as winds, with periods dependent on the season (Banfield et al., 2020; Forget et al., 2019). The LDS did not produce appreciable effects on the mean pressure; however, the diurnal pressure amplitude range within each sol experienced a strong increase, mostly due to the effect of the LDS on the thermal tides. This is common to other storms observed by the Viking Landers (e.g., Ryan & Henry, 1979; Ryan & Sharmann, 1981) and MSL (Guzewich et al., 2016, 2019; Ordóñez-Etxeberría et al., 2019; Viúdez-Moreiras et al., 2019) (see section 4).

Preliminary mean air temperature estimates, using T_{air}, ranged from 205 to 210 K. Very similar results are obtained if T^p_{air} is used instead (Figure 4). Minimum ground temperatures increased by ~5 K (~188 to

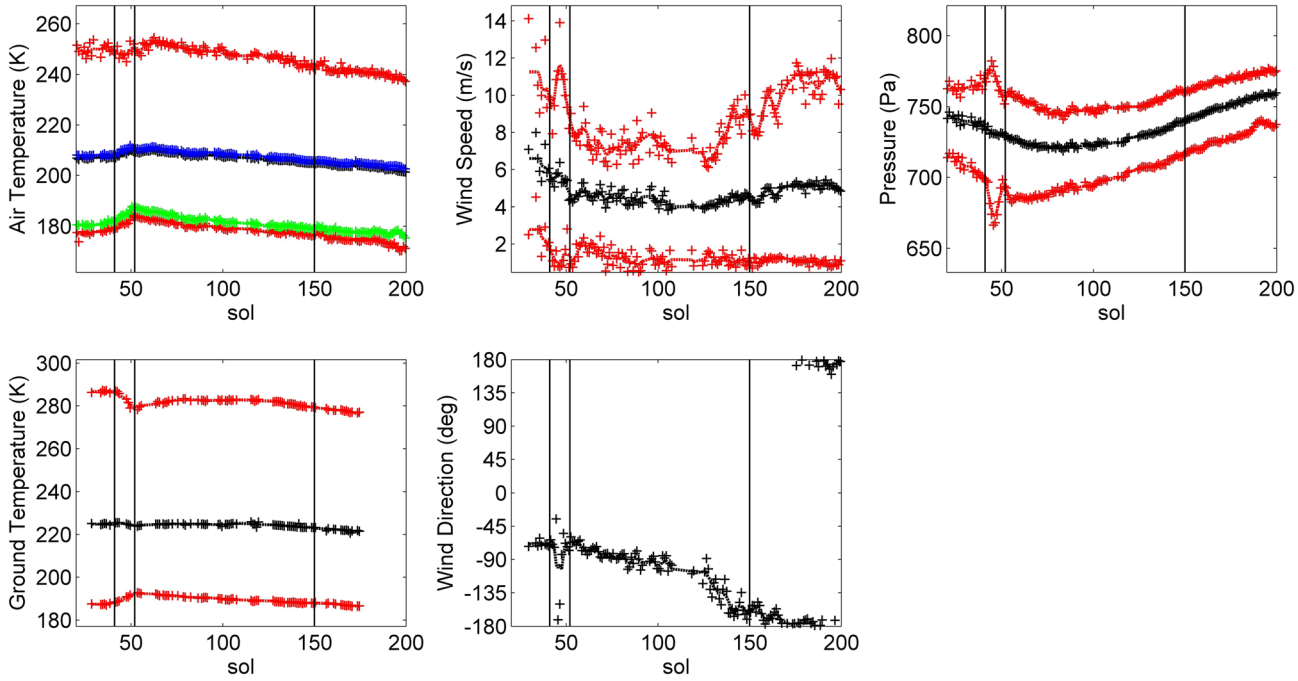


Figure 4. Evolution of APSS/HP^3 variables (Sols 0–200) for the period encompassing the onset, growth, and decay phases of the MY34 LDS. Vertical lines show the start times of LDS onset (Sol 41, L_s ~ 320°), maximum optical depth at InSight's landing site (Sol 52, L_s ~ 326°), and when opacities return to seasonal levels (Sol 150, L_s ~ 18°). Daily mean, minimum, and maximum values are shown for air and ground temperature (a and d, respectively), wind speed (b), and pressure (c), while (e) shows the direction from which the wind blows (in degree clockwise relative to N; see Figure 1) and presents only the daily mean wind directions. Sols before Sol 18 contain gaps in some diurnal timeslots due to the instruments still being in the commissioning phase; therefore, their daily mean values are not shown as they would be biased toward certain times of sol. A wide gap also covers some sols in the Sol 108 to 123 range, mostly affecting wind data, due to APSS instrument issues. Air temperature, T_{air}, is estimated using Temperature Estimation Method A (see section 2). Minima air temperatures using T_{night} (Temperature Estimation Method B) and daily mean temperatures using T^{p}_{air} (see section 2) are also shown for comparative purposes in green and blue, respectively. A 4 sol running average is also shown in each case.

~193 K), and minimum air temperature estimates increased accordingly (~179 to ~184 K and ~183 to ~188 K, using T_{air} and T_{night} estimates, respectively; see section 2) and peaked at Sol ~50, in accordance with the peak in τ, as a consequence of the higher atmospheric dust load, and hence warmer air masses than usual at night, lowering the IR radiative cooling of the surface. On the other hand, maximum ground temperatures decreased by ~9 K (~287 to ~278 K) over the same period, as a result of greater solar radiation absorption and scattering by the atmosphere, which decreased the surface insolation. These effects were also observed during previous storms (e.g., Guzewich et al., 2019; Ryan & Henry, 1979; Ryan & Sharmann, 1981; Tillman, 1984; Wilson & Richardson, 2000). Minimum ground temperatures over a sol appeared higher than minimum air temperatures over the entire mission, which is the contrary that we expect from theory and from observations from previous missions. However, the air temperature signal can be strongly perturbed by lander thermal effects (section 4.2), and thus, it represents the *local* air temperature, not the *far field* atmospheric air temperature. In short, InSight's platform produces an increase in the estimated air temperature during the day and a decrease during the night. This effect was also observed in the close field observed by HP^3-RAD, and it is the reason we selected the far-field observations of this instrument, which are less perturbed by the lander (see section 2), as the *ground* temperature. Maximum air temperatures were roughly constant as the LDS evolved, slightly decreasing during the storm's onset and peaking at Sol ~60, as described in detail in section 4. Mean ground temperatures remained roughly constant within the LDS period. Daily mean air temperatures followed a similar evolution to the minima, although with a smaller variation of ~3 K, which is comparable to the sensor's accuracy.

The most dramatic variability during the northern winter and spring seasons was observed in the near-surface wind patterns. Winds were west-northwesterly in the daily mean (Figure 4) at the beginning of the mission, as a result of the Hadley cell that dominates in northern winter, with upwelling motion in

the summer (southern) hemisphere, downwelling in the northern hemisphere, and a return flow (from north to south) across the equator at low levels. These zonal-mean ~northerly flows are strongly perturbed in the region of InSight (Figure S1) by the channeling effects of the regional topography at InSight's general location in Elysium Planitia, that is to say, the dichotomy boundary and Elysium Mons. This behavior was predicted by GCMs (Figure S2, adapted from Figure 9 in Spiga et al., 2018), although with an ~15° offset between the predicted and observed wind direction. Oscillations in the diurnal-mean scenario due to baroclinic waves, with a variable period dependent on season, are also found in the wind and pressure signals (Banfield et al., 2020; Forget et al., 2019).

The onset of the LDS (Sols 44–48) strongly modified wind speeds and directions, modifying the diurnal-average wind direction to south-southwesterly, strongly increasing the diurnal-maximum wind speeds (from ~10 to ~14 ms^{-1}) and decreasing the diurnal-minimum wind speeds by ~1 ms^{-1}, resulting in a slight increase in the average wind speeds of ~1 ms^{-1}. Long after the LDS's peak, the diurnal-average winds rotated to westerly as the fall equinox approached (Sol ~114), due to the northerly component decreasing as the zonal-mean large-scale circulation transitioned from a single, strong solsticial Hadley cell to a dual-Hadley cell, weaker equinoctial circulation. In fact, the diurnal-average wind speeds decreased from ~ 8 m/s on Sol 20 (L_s ~ 307°) to 4.5 m/s in Sol 114 (L_s ~ 0°). As the season evolved further, another solsticial circulation developed but with the direction of the Hadley circulation reversed, producing near-surface flows in the opposite direction (i.e., ~southerly surface winds). During this season, numerical models predict that the large-scale ~southerly flows are strongly perturbed by the regional topography around InSight's general location, thus producing a similar channel effect as in northern winter, but in the opposite direction (Figure S2 and see also Spiga et al., 2018), which is confirmed by InSight data. As a result, mean south-southeasterly winds were observed by InSight (Figure 4), with lower intensities than those reached by the strong near-surface winds observed in the first sols of the mission. The knowledge of this evolution under *nominal* conditions is very useful to understand the effects on the wind patterns of the LDS, as will be described in section 4.

4. Diurnal Cycles at Elysium Planitia

This section presents the effect of the LDS on the diurnal cycles of meteorological variables observed by InSight. Figure 5 shows the diurnal cycle for air temperature (T_{air}), wind speed, pressure, ground temperature, and wind direction as a function of LTST. Sols 37–41 (L_s ~ 319°) before the storm are compared with Sols 44–48 (L_s ~ 323°) at the end of the onset of the LDS, which, as shown in Figure 4, is when the storm's impact on pressure and winds was the greatest and is also very close to the maximum disturbance in air and ground temperatures (Sols 50–54, L_s ~ 326°). This period is also shown in Figures 5e and 5f for air (T_{air}) and ground temperatures, respectively. Figure S3 presents the diurnal evolution of the same variables during Sols 35–90 (L_s ~ 316–347°).

4.1. Pressure Cycle

The diurnal pressure cycle is mainly driven by the global thermal tides (Hess et al., 1977; Leovy & Zurek, 1979; Wilson & Hamilton, 1996; Zurek & Martin, 1993) and is modulated by the presence of dust loading, topography, surface albedo and thermal inertia, and water ice clouds (Kleinböhl et al., 2013).

The thermal tide response in the Mars atmosphere is usually dominated by the diurnal mode in low-dust-loading conditions and by the semidiurnal mode in high-dust-loading circumstances (Hess et al., 1977; Leovy & Zurek, 1979; Lewis & Barker, 2005; Wilson & Hamilton, 1996; Zurek & Martin, 1993). The frequency-domain behavior of surface pressure detected by a station is the result of overlapped migrating and nonmigrating tides, the latter being mainly the nearly resonant Kelvin wave (Zurek, 1976; Zurek & Leovy, 1981). These migrating and nonmigrating tides cannot be decoupled either using observations from a single station (InSight) or even using simultaneous observations from two nearby locations at similar longitudes (InSight and MSL), given the uncertainty in capturing the longitudinal dependence of the tidal oscillations and hence the nonmigrating tidal response.

Before the onset of the storm, surface pressure exhibited a significant diurnal cycle (Figure 5) ranging from 698 to 768 Pa (diurnal range of ~70 Pa) at Sol 40 (L_s ~ 319°). The diurnal range suddenly increased during the onset of the LDS and reached ~112 Pa on Sol 45 (L_s ~ 322°), ranging from 666 to 778 Pa (Figure 5). Figure 6

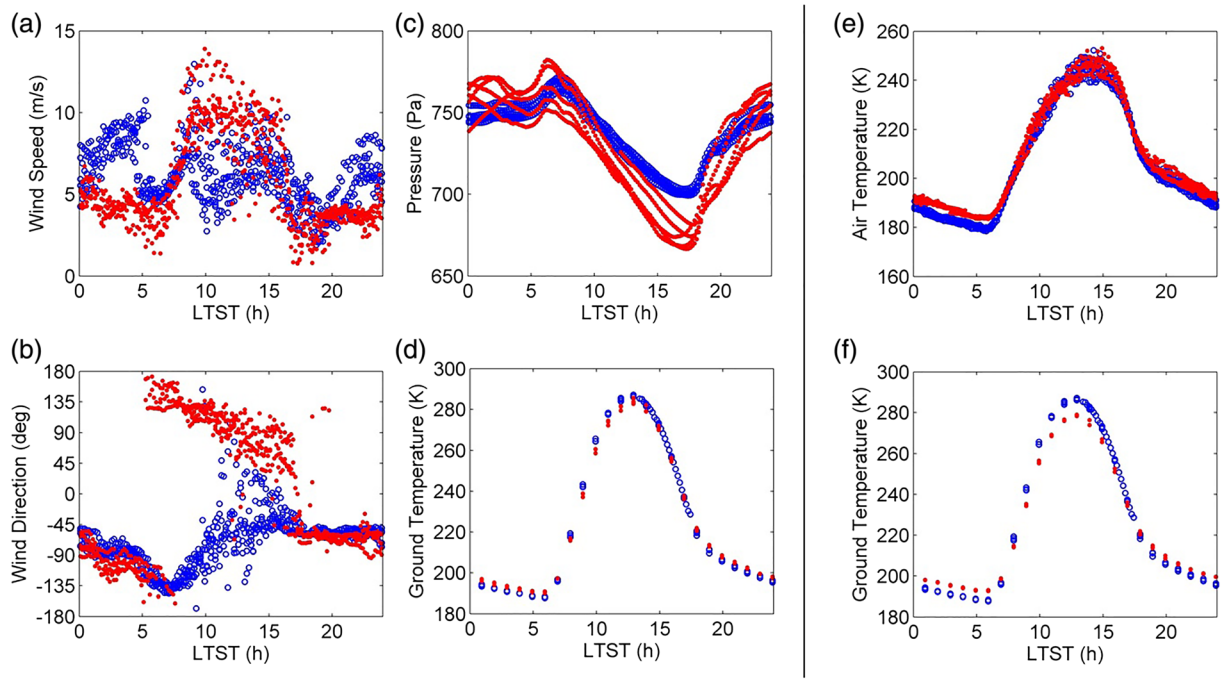


Figure 5. (a–d) The diurnal cycles for wind speed and direction, pressure, and ground temperature as a function of Local True Solar Time (LTST), shown for five sols before (open blue circles, Sols 37–41, L_s ~ 319°) and during (red dots, Sols 44–48, L_s ~ 323°) the onset of the LDS. (e and f) Similar panels but showing air (T_{air}) and ground temperatures comparing between Sols 37–41 and the period around the opacity peak (Sols 50–54, L_s ~ 326°).

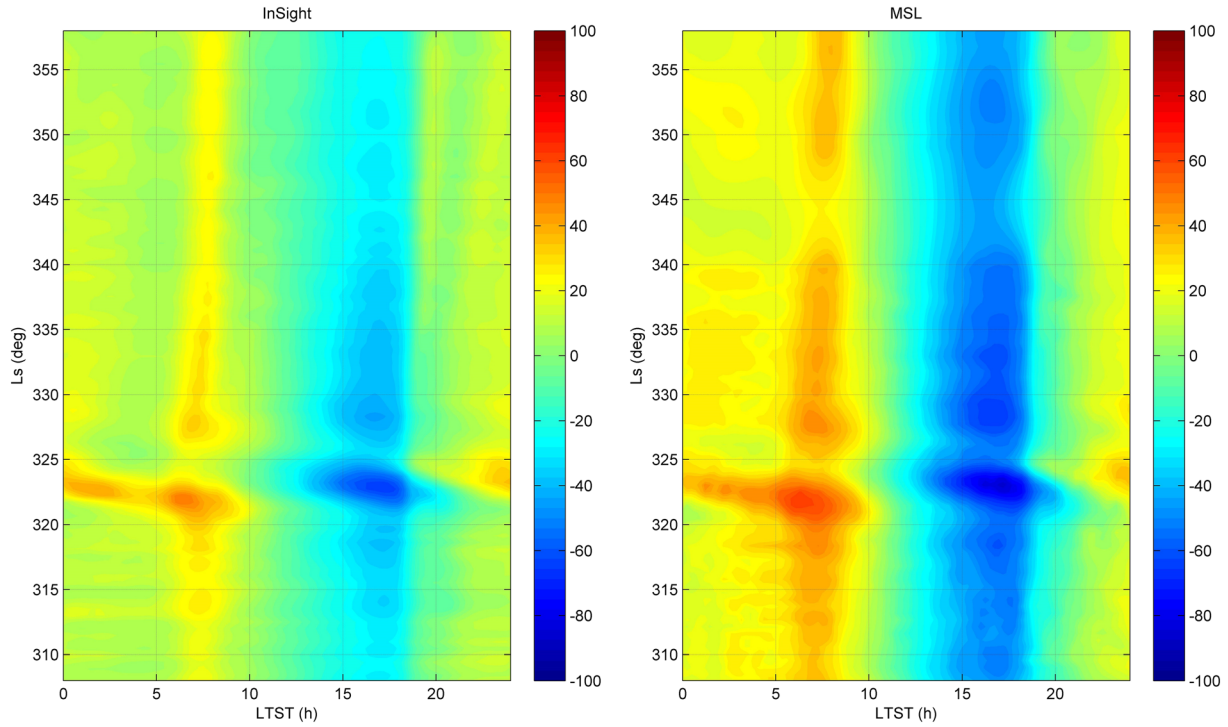


Figure 6. Evolution of the thermal tide signature (Pa), as seen in the pressure diurnal anomaly (computed as instantaneous pressure minus its daily mean), as a function of areocentric solar longitude (L_s) and Local True Solar Time (LTST), both for InSight (left) and MSL (right) pressure data. InSight Sol period corresponds to 20–110. Note the enhanced effect in pressure diurnal anomaly detected by MSL (see text).

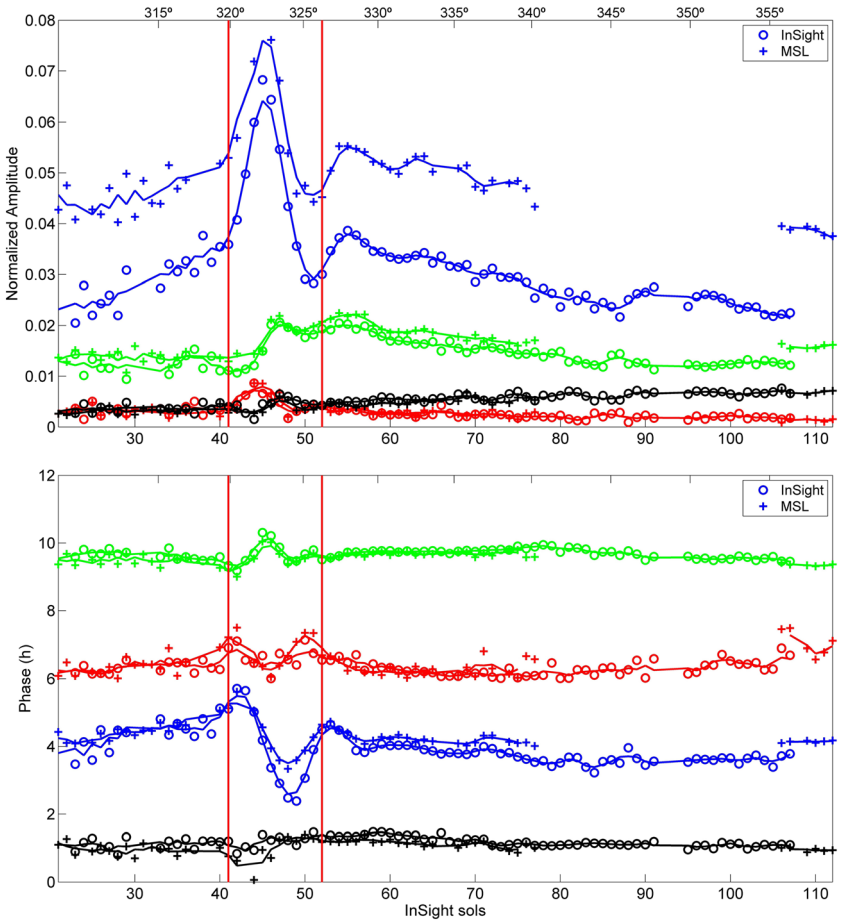


Figure 7. (top) Evolution of the diurnal pressure mode normalized amplitude (blue), compared to the semidiurnal (green), terdiurnal (red), and quadiurnal (black) mode amplitudes for InSight's landing site (circles) and MSL (crosses) in the sols enveloping the dust storm; (bottom) as in the top but for the pressure mode phases. Also shown is a 4 sol running average. Note that pressure amplitudes are normalized to the mean daily pressure for each landing site. L_s is also included in the horizontal axis for comparative purposes. MSL experienced two technical issues between $L_s \sim 340°$ and 353°, losing most of data during these periods. Vertical lines show the start times of LDS onset (Sol 41, $L_s \sim 320°$) and maximum optical depth at InSight's landing site (Sol 52, $L_s \sim 326°$).

shows the evolution of the surface pressure during the dust event, as a function of local time and areocentric solar longitude, by showing the instantaneous pressure on each time of the sol minus its daily mean. This enhancement is clearly shown in this figure during the onset of the LDS. A clear double-peak structure in the pressure cycle can be observed at the end of the onset (Figures 5, 6, and S3), due to the different tidal signature, particularly the enhancement of the semidiurnal pressure mode after the partial recovery in the diurnal pressure range (it fell back to 58 Pa on Sol 50 [$L_s \sim 325°$]; Figures 5 and 6), hence increasing the weight of this pressure mode in the diurnal cycle.

The effects of the dust storm can be analyzed in more detail by means of pressure harmonics analysis. Figure 7 presents the normalized amplitudes and phases for the first four pressure modes (diurnal, semidiurnal, terdiurnal, and quadiurnal) as a function of sol of the InSight mission and shows a comparison with the pressure modes acquired by MSL at Gale crater during the first period of the LDS. It can be observed that the diurnal mode amplitude was roughly twice as large at MSL's location prior to and after the storm. This is because the diurnal pressure mode is strongly amplified in Gale crater by topography (Guzewich et al., 2016), possibly by hydrostatic adjustment flows (Richardson & Newman, 2018). The semidiurnal pressure mode amplitude was also higher at MSL's location, suggesting asymmetries in the latitudinal variation or a topographic effect, given that the semidiurnal tide mode is mostly symmetric across the equator (e.g., Lewis &

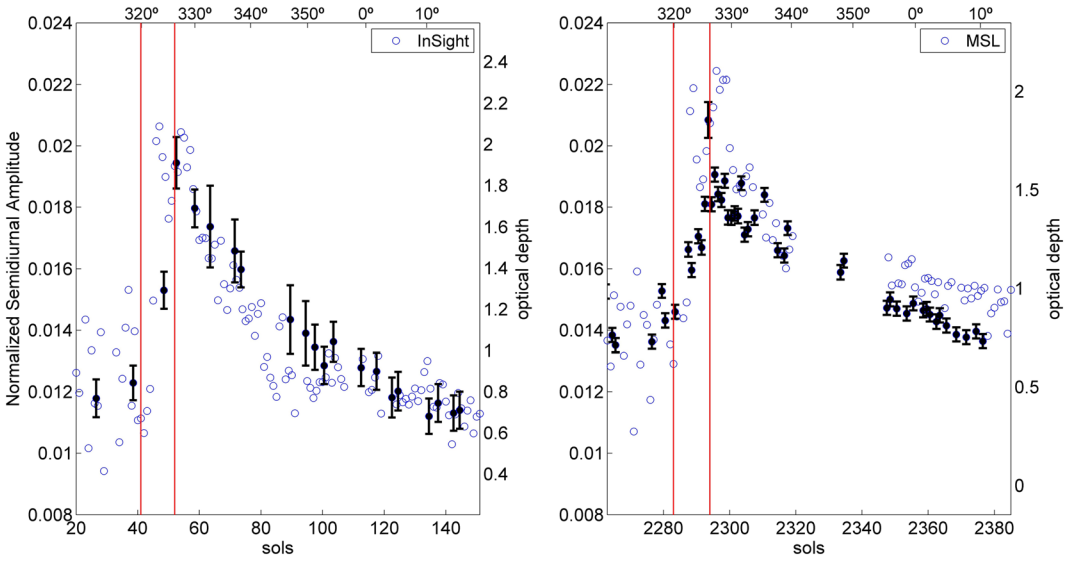


Figure 8. Comparison between atmospheric opacity measured by InSight's (left) and MSL's (right) cameras (Lemmon et al., 2019), as a function of sol (black dots and with their error bars), and the semidiurnal pressure mode amplitude (blue dots) measured by each mission. Both panels cover the same period of sols (note that the left panel is a function of InSight Sols and the right panel of MSL Sols). MSL experienced two technical issues between L_s ~ 340° and 353°, losing most of the data during these periods. Vertical lines show the start times of LDS onset (InSight Sol 41, L_s ~ 320°) and maximum optical depth at InSight's (and MSL) landing sites (InSight Sol 52, L_s ~ 326°).

Barker, 2005). Diurnal and semidiurnal pressure phases were similar between both missions in accordance with tidal theory (Guzewich et al., 2016; Lewis & Barker, 2005). Terdiurnal and quadiurnal modes presented similar values and behavior in both missions.

Pressure tides were strongly affected by the LDS. Each pressure mode showed a different behavior during the event. Just prior to the storm, the diurnal pressure mode's normalized amplitude (to the mean daily pressure at InSight's location) (~0.025) was roughly twice the semidiurnal amplitude (~0.012) prior to the LDS and much higher at MSL's location as described above. The diurnal amplitude then experienced an abrupt increase during onset of the LDS at both locations, peaking to 0.070 and 0.075 on Sol 45, but recovered their prestorm values with an oscillatory behavior a few sols later. The diurnal pressure mode's phase was also significantly disturbed during storm onset, varying by almost ±2 hr (Figure 7) at both locations, with a larger effect at InSight's location than in Gale crater, possibly due to topographic influences. Enhancement of the diurnal mode amplitude was also observed in the tidal analysis of data during the two 1977 GDSs from the Viking Landers (e.g., Zurek & Leovy, 1981) and in regional and local storms by MSL (Guzewich et al., 2016; Ordóñez-Etxeberría, Hueso, Sánchez-Lavega, & Vicente-Retortillo, 2020). The transitory amplitude and phase disturbances of the diurnal pressure mode observed during the storm onset can be attributed to an enhancement of the nonmigrating Kelvin wave due to spatial asymmetries in the atmospheric dust abundance (Wilson & Hamilton, 1996; Zurek & Leovy, 1981), and it was observed during the 1977B GDS as well (Wilson & Hamilton, 1996; Zurek & Leovy, 1981). The observed behavior during the LDS also presents similarities to the observed response by MSL during the onset of the MY34 GDS (Viúdez-Moreiras et al., 2019), in which there were strong transitory amplitude and phase perturbations of the diurnal pressure mode, although the amplitude and phase disturbances of the GDS lasted more than 40 sols. Also, in the MY34 GDS case, the diurnal pressure amplitude was later strongly reduced because of a further reduction in the nontidal topographical component in Gale crater (Guzewich et al., 2019) due to the widespread reduction in the diurnal air temperature range caused by the storm (Figure 5 in Viúdez-Moreiras et al., 2019).

The semidiurnal pressure mode amplitude increased and decreased with τ during the LDS at both InSight and MSL (Figure 8), as expected from the theory described above and in accordance with previous analysis showing a good correlation between the semidiurnal pressure mode amplitude and dust opacity (Guzewich et al., 2016; Hess et al., 1977; Leovy & Zurek, 1979; Lewis & Barker, 2005; Wilson & Hamilton, 1996; Zurek &

Martin, 1993). While the pressure tide signature responds to the regional-to-global atmospheric dust distribution rather than the local dust column, there is typically high correspondence between the local atmospheric optical depth measured by surface missions and the larger-scale dust abundance. Exceptions occur if the surface mission is located far from primary dust lifting centers at any stage of the storm and/or if local topography slows transport of dust into or out of the region. For example, during the MY34 GDS, the diurnal amplitude and the diurnal and semidiurnal phases measured by MSL-REMS responded three sols before the local opacity measured by MSL-Mastcam at storm onset, due to the dust storm initiating halfway around the planet, while later, the semidiurnal amplitude peaked even as the local opacity was decreasing, due to a second surge of regional and global dust increases that did not appear to reach (or penetrate) Gale crater (see Figure 5 in Viúdez-Moreiras et al., 2019). For the LDS measured both by InSight and MSL, however, the bulk of the semidiurnal tidal response appears to be more or less aligned with the opacity peak measured by both missions, with no clear "anticipation" or shift to the local dust opacity observed either in tidal amplitudes or phases. Gaps present in the opacity measurements make it difficult to absolutely confirm this, however (there were no opacity measurements until 7 sols after the pressure responded) (Figures 7 and 8).

In both missions, the terdiurnal pressure mode amplitude was significantly enhanced during onset of the LDS and peaked 1 day before the diurnal pressure mode amplitude (Figure 6). The terdiurnal tide presents a more complex structure than the diurnal and semidiurnal tides. On Earth, it shows strong hemispheric asymmetry, particularly in midlatitudes, driven by the sensitivity of the propagation to the background state (e.g., Smith & Ortland, 2001). In addition to direct solar forcing, this tide is also excited by nonlinear interactions between the diurnal and semidiurnal pressure modes, particularly in low latitudes (Smith & Ortland, 2001; Teitelbaum et al., 1989). These mechanisms could also be involved in the observed response in the lower Martian atmosphere. The strong differences in atmospheric dust content produced by the storm (Figure 3), leading to hemispheric thermal gradients during the storm onset (section 3.1), in addition to the LDS perturbation in the diurnal and semidiurnal tides (Figure 7), could be responsible for enhancing the terdiurnal mode during the LDS onset, similar to the effect observed during the MY34 GDS. However, the amplitude mode response quickly returned to prestorm values following the onset period of the storm, which strongly differs from the response observed during the MY34 GDS, where it followed closely the evolution of the semidiurnal mode amplitude. This is potentially due to the decay period of the LDS being relatively short, helping to reestablish the prestorm values. The quadiurnal pressure mode amplitude evolved as the mission progressed from ~2 to ~5 Pa, contributing to the diurnal pressure cycle observed after the storm (Figures 5 and S3).

4.2. Air and Ground Temperature Cycles

Measured air temperatures ranged from ~175 to ~255 K (Figures 5 and S3) but, as described in section 2, are likely strongly perturbed by the lander, making the local temperatures measured by both booms quite different from the real atmospheric temperature. The retrieved atmospheric temperature, T_{air} (see section 2), can minimize the lander's thermal contamination but does not remove it completely.

The ground responds first to solar heating with temperatures peaking at ~12:00–13:00 LTST (Figure 5). The near-surface air has a higher thermal inertia than the surface and is heated more by the surface than directly; hence, maximum near-surface air temperatures were measured at ~14:00–15:00 LTST. The midday (MD; 10:00–15:00 LTST) and afternoon (15:00–18:00 LTST) timeslots are also characterized by strong convective turbulence (see section 5) driven by large surface-to-air thermal gradients, which are probably enhanced near the lander platform due to the higher platform temperatures reached during the day, particularly in the solar panels (solar panel sensors show temperatures reaching ~290 K).

During the day, the temperatures retrieved by both TWINS booms (T_{local1} and T_{local2}), installed on the west and east sides of the lander and pointing to the west and the east, respectively (Figure 1), are strongly affected by the lander's thermal contamination and can be strongly affected by wind patterns. If the wind direction comes from the front of a particular boom, the temperature is expected to be less perturbed than if the wind direction comes from the rear of the boom, because in the latter case, (a) the loss of efficiency in heat transfer between the air and the boom affects the retrieved temperatures (see section 2) and (b) the air masses affecting the sensor have previously flowed over the lander platform and are disturbed due to the greater-than-air platform temperatures. Also, low wind speeds decrease the heat exchange by convection and increase the error in the estimated temperatures. The result of this combined effect can be seen in Figure 9, which

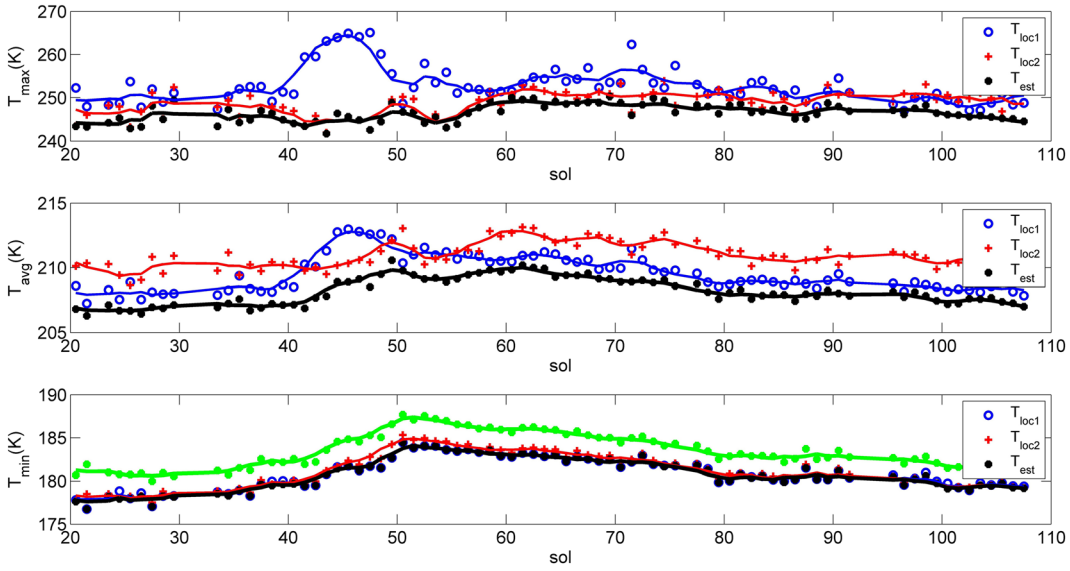


Figure 9. Trend in maximum, diurnal-average, and minimum air temperatures measured by both booms (T_{local1}: westward-facing boom; T_{local2}: eastward-facing boom) and preliminary estimation of air temperature (T_{air}, based on Estimation A in black) (see text). Minimum temperature computed from T_{night} is also shown for comparative purposes in green (see section 2). Temperatures shown in the figure are computed from 10 min average T_{local1} and T_{local2} measurements. Also shown is a 4 sol running average. T_{air} efficiently minimizes the observed overheating (~15–20 K, see text) during the day. T_{night} partially reduce the lander's overcooling during the night (~10 K, see text), although it does not remove it completely. Both are major problems for interpreting the raw temperature measurements.

shows the retrieved local temperatures at both booms, T_{local1} and T_{local2}, differing in their daily mean values by at least 2 K over the whole period. The maximum temperatures show more similarity, although this is due to the strongest winds typically occurring during the MD and afternoon timeslots, when a large percentage of winds, which present great dispersion (Figure 5), are from ~NW-NNW, hence approach both booms roughly from the side (Figure 2). During the onset of the LDS, wind patterns changed within the MD timeslot, from northwesterlies with a high variability in wind direction to easterlies with a lower variability in wind direction (Figure 5). The maximum temperature from T_{local1} rose to 15 K and occurred at ~13:00 LTST, as air now approached it from the rear, thus (a) wind speeds (hence heat transfer) over the sensor decreased and (b) air parcels reaching it had been disturbed by passing over the lander body for the reasons described above. Conversely, the maximum temperature from T_{local2} decreased and occurred 1 hr later, at ~14:00 LTST, a timing that is far more consistent with the air being warmed by the surface. The estimated air temperature, T_{air}, which uses the lower of the two measured values during the day, is thus largely based on T_{local2} during this period. Also, daytime air temperatures could be overestimated during periods of weak and highly variable winds. This pernicious effect in the booms' temperatures may also be used to retrieve information about the wind patterns, which can be particularly important for missions that do not include a WS or if the WS fails, such as on the MSL rover at Sol ~1491 (Viúdez-Moreiras et al., 2019b). In the case of MSL, in addition, the thermal contamination comes also from the RTG, which strongly influences the temperature field around the rover (Gómez-Elvira et al., 2012).

During the nighttime, despite the dust opacity during the LDS ($\tau < 2$) being far below the peak values observed during the MY34 GDS by MSL (Lemmon et al., 2019), the minimum air and ground temperatures, reached immediately predawn at ~06:00 LTST, were significantly affected as a consequence of the increase in τ. This increase prevented an efficient nighttime IR radiative cooling from the surface, leading to warmer surface and near-surface air masses. Thus, the surface was warmer in the dust storm period at night, and minimum air and ground temperatures evolved accordingly with τ (Figures 3 and 4), reaching their maximum on Sol 51. Nighttime air temperatures were ~9 and ~5 K colder than ground temperatures using T_{air} and T_{night} estimates, respectively (a similar difference was also observed between the far and the close spot of HP^3-RAD, with the close spot measurements being colder than the far spot measurements), suggesting

that the lander's thermal contamination is inducing a strong bias during the night that is not completely removed even by using the T_{night} estimation (Figure 9), with the rapidly cooling (very low thermal inertia) solar panels producing a strong cooling of the air above them. The similar values in the booms' nighttime temperatures, independent of wind direction, suggest that radiative heat transfer dominates at night, instead of the more influencing convective heat transfer during the day, which is compatible with the very low surface-to-air thermal gradients (<10 K) in comparison with those reached during the day (>40 K), and the lower wind speeds during the night.

The net LDS effect on the daily mean air temperatures is a warming influenced by the higher nighttime temperatures (which rose ~5 K, similarly to the ground temperatures; Figures 4 and 9), linked to the dust opacity (Figure 3f). In any case, the observed daily mean temperature difference is small (~3 K) and could be influenced by errors derived from the aforementioned effects. Similar effects in air and ground temperatures were obtained by MSL in Gale crater during the opacity peak of the LDS ($\tau < 2$), which contrast with the strong perturbation by the MY34 GDS ($\tau \sim 8.5$) (Figure S4).

4.3. Diurnal Cycle of Wind

A large set of wind data was obtained from the InSight WS, enabling the diurnal cycle of wind speed and direction in local winter to be determined for InSight's landing site in Elysium Planitia. Given the complexity in the observed wind patterns by InSight, we start this section by describing the diurnal cycle of wind observed prior to the LDS onset. Later, we present the observed diurnal cycle under dust storm conditions and compare it to the diurnal cycle under nominal conditions. Finally, we describe the evolution of the wind pattern during the LDS decay, which overlapped with the expected seasonal evolution.

We expect that the diurnal cycle under nominal conditions, that is, without the effect of a dust storm, is produced by a combination of the interaction of the large-scale Hadley circulation and thermal tides with regional and local effects induced by topography, which combine to produce a diurnal perturbation superimposed on the mean scenario described in section 3. The relatively flat areas in which the Viking Landers (VL1 and VL2) landed can offer insights into the wind patterns observed by the InSight mission prior to the LDS. VL1 and VL2 obtained wind data on two separate locations at latitudes 22.5° and 48.0°, respectively. Wind data analysis suggested the diurnal cycle of winds at VL1 and VL2 landing sites to be the result of the aforementioned interactions (Hess et al., 1977; Leovy & Zurek, 1979; Wilson & Hamilton, 1996). Thus, a counterclockwise rotation was found in the VL1 wind data in early summer (Hess et al., 1977), with the sense of the rotation differing from the clockwise rotation observed by VL2 and changing later in the mission. The behavior observed by VL1 was attributed in Hess et al. (1977) to a combination of near-surface slope flows, peaking in the midafternoon, and maximum turbulent coupling with the winds aloft, peaking in late afternoon. At the VL2 landing site, it was unnecessary to invoke coupling to winds aloft to explain its clockwise rotation pattern. Thus, there was no need to invoke interactions with large-scale diurnally varying pressure fields by thermal tides. Also, Leovy and Zurek (1979) analyzed the VL2 wind data and found that the clockwise rotation observed in the diurnal wind pattern did not agree with the expected phases of a diurnal westward propagating tide. However, they found a clear effect from the semidiurnal mode of the thermal tides on the surface wind pattern after the enhancement of this mode during the 1977 GDSs.

The diurnal wind pattern observed by InSight under nominal conditions at northern winter is mainly attributed to regional and local effects induced by InSight's landing site slope and probably by the regional dichotomy boundary (Figure S1) rather than by thermal tides. For example, at landing time, InSight had winds from ~NW over much of the sol except for between ~1 and ~10 a.m., when winds turned to come from the SW (shortly before ~06:00) and back again. This timing is very suggestive of control by nighttime downslope winds, which increase overnight and peak at around dawn, and indeed, GCM simulations performed with an artificial removal of the general landing site slopes (and keeping the tidal signature) mostly remove the diurnal cycle observed by InSight (Figure SM2 in Banfield et al., 2020). It is important to highlight how the very small slope angle of the regional terrain (<0.1° downward ~50° of azimuth, clockwise from the north), similar to VL1's general slope, is enough to induce slope winds significant enough to shape the diurnal cycle.

Figure 10 shows the diurnal cycle of winds before, during, and after the LDS by means of hodographs, which complements Figure 5 (showing the disturbance in wind speed and direction). We start by

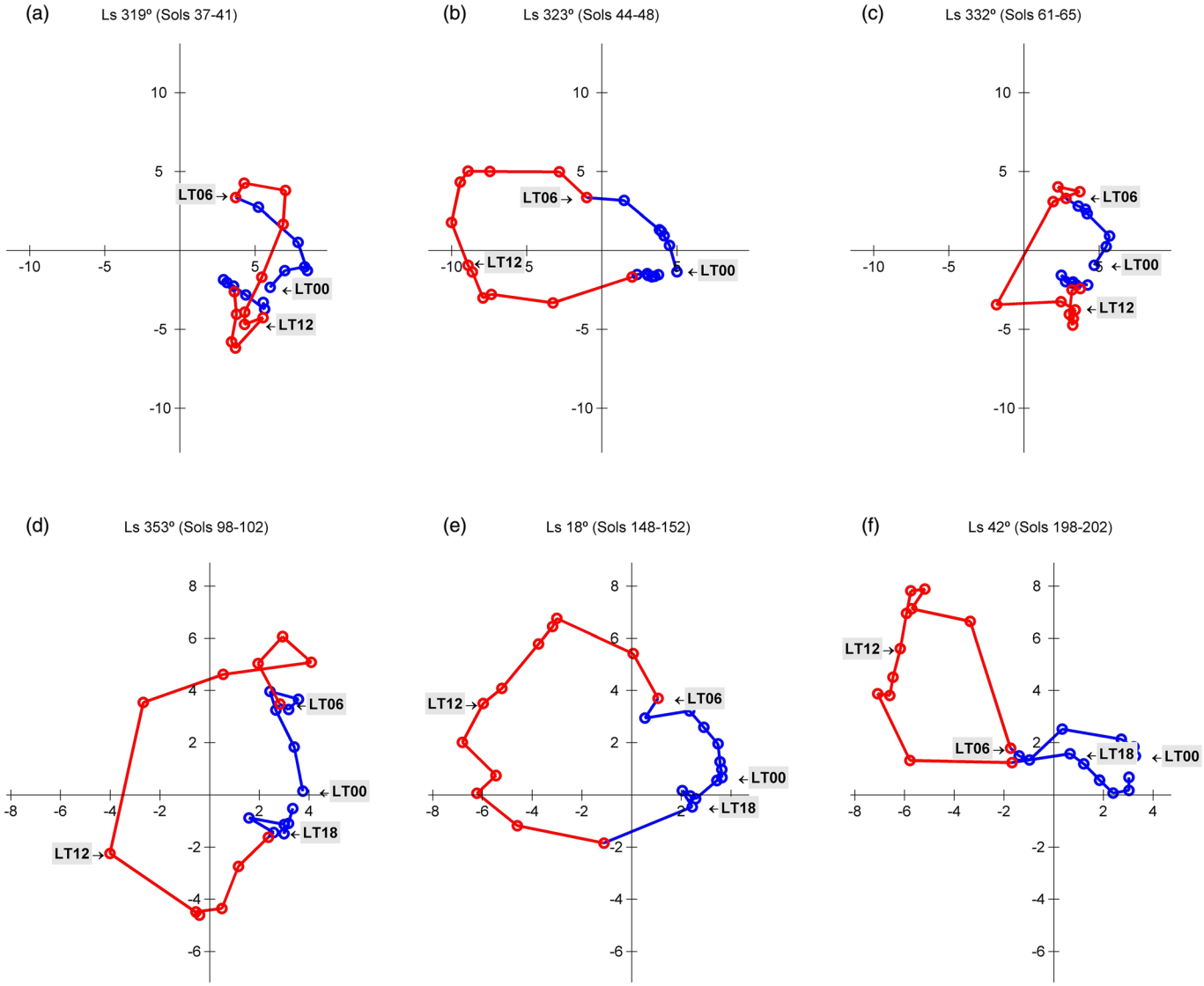


Figure 10. Wind hodographs based on hourly-mean winds (m/s) in 5 sols during the dust storm period and the northern winter and spring seasons. (a) Pre-LDS during northern winter, (b) LDS onset, (c–e) LDS decay (L_s ~ 332°, 353°, and 18°), and (f) northern spring (L_s ~ 42°). The mean wind vector at each time is given by a vector from the origin of coordinates to the point shown for each time of sol. Note the contrast with the wind directions in Figure 5, which show the direction from which the wind is blowing, following the standard meteorological convention. The 6–17 LTST values are colored in red and 18–5 LTST in blue for a better visualization of the ~daytime and ~nighttime periods, respectively.

describing the observed diurnal cycle of winds under nominal dust conditions. Prior to the storm on Sols 37–41 (Ls ~ 317–320°), winds were northwesterlies at midday, as ~northerly anabatic upslope flows toward the dichotomy boundary were constructively coupled with the ~northwesterly Hadley flow. A pronounced short-term variability (Figure 5) was observed both in wind speed and direction, due to convective turbulence as the ground-to-air thermal gradients developed during the daytime. Wind direction variability was strongly reduced in the afternoon (Figure 5b; ~15:00 LTST), and wind speeds increased (Figure 5a). In the evening, observed wind speeds decreased again as upslope winds reduced their strength. These effects can also be observed in Figure 10a. Winds remained northwesterly during the first part due to the ~northerly Hadley flow and its channeling by regional topography (section 3). The measured wind speeds ranged between 5 and 8 m/s between 0:00 and 2:00 LTST. At ~5:00 LTST, wind speeds abruptly decreased to 5 m/s. The increase and the further abrupt decrease in wind speeds at ~5:00 LTST could possibly be due to interference between the Hadley cell return flow, the downslope winds,

and the tidal flows but also due to enhancement of local winds by lander perturbations (see section 2) or WS issues, which remain to be investigated. This enhancement in wind speed before 5:00 LTST prior to the storm is not reproduced by mesoscale and GCM models to date. Winds rotated to come increasingly from the ~SW in the early morning (up to ~7:00 LTST) as downslope katabatic winds (due to the aforementioned local slope) grew stronger, matching the timing of the maxima in the pressure diurnal cycle (Figure 5c), suggesting that the effect of the downslope flows reached a maximum right around dawn (~6:00 LTST for this season and latitude). Near-surface winds quickly rotated again but with a clockwise rotation and returned to their original heading before 10:00 LTST (Figure 5b). Wind speeds were increased to as much as 13 m/s at ~8:00 LTST, reaching the maximum wind speeds observed within the diurnal cycle (note that these values correspond to 10 min average values, and therefore, higher values occur on shorter timescales).

The asymmetry in the diurnal pattern of the meridional wind component, that is, winds with a higher northerly component during the daytime than those reached by the southerly component of the winds during the nighttime (Figure 10a), can be attributed to two processes acting together: (i) the meridional component of the ~northeasterly anabatic upslope flows acting constructively with the large-scale meridional component of the ~northwesterly Hadley circulation, whereas the downslope flows combine destructively; and (ii) the greater expected coupling between surface winds produced mainly by topography and the winds aloft, as the planetary boundary layer is developed during the daytime. In this sense, the reduction (or perhaps entire lack) of significant coupling during the nighttime could have allowed ~southerly downslope slope flows to develop producing the observed winds (Figure 10a), opposite to the general circulation, although modeling would be needed to support this hypothesis.

Wind patterns changed completely within the LDS period. Figures 5 and 10b present the observed wind patterns during the onset of the LDS (Sols 44–48, L_s ~ 322–324°) and showed dramatic deviations from the winds previously observed. These changes are in accordance with the enhancement in the thermal tides; we remind the reader (see section 4.1) of the strong enhancements in the diurnal and semidiurnal pressure tidal mode amplitudes, especially the diurnal, and disturbances in their phases (Figure 7). Winds during this period described a complete and marked counterclockwise rotation over the sol, starting at midnight (Figure 10b). Surface winds were west-northwesterly at that time (Figures 5 and 10b), similar to the prestorm values, with measured wind speeds dropping significantly below prestorm values (to 4–6 m/s) between 0:00 and 2:00 LTST. Wind speeds remained low until 07:00 LTST and continued the counterclockwise rotation started at midnight. At 07:00 LTST, winds had rotated to southwesterly, and they continued the counterclockwise rotation to east-northeasterly, while wind speeds abruptly increased from 2–4 to 10–14 m/s at 10:00 LTST. The rotation, and the high wind speeds, continued until ~15:00 LTST, when speeds decreased to 2–4 m/s and wind directions changed more abruptly from northeasterly to northwesterly. As the storm evolved, on Sols 61–65 (L_s ~ 333°), the wind diurnal cycle returned to the prestorm behavior despite the dust loading still being high. Later, as mentioned in section 3, the wind pattern evolved with the season.

The observed impact of the dust storm on the wind pattern can be explained by different mechanisms. A sudden increase of dust loading can have several effects on surface winds: (i) It can enhance the intensity of the hemispheric thermal gradient and thus enhance the Hadley cell circulation (e.g., Basu et al., 2006; Heavens et al., 2011; Kass et al., 2016); (ii) it can modify the static stability of the atmosphere (e.g., Zurek, 1976) and thus the effect of the boundary layer on the surface winds; and (iii) it can increase the strength of the thermal tides and thus of the winds induced by these planetary-scale waves (e.g., Wilson & Hamilton, 1996; Zurek & Leovy, 1981).

Right away, we can state that Hypotheses (i) and (ii) are not supported alone for this particular storm by the timing of the wind changes that occur during the onset of the LDS and nor during the entire period of high dust loading. Furthermore, Hypothesis (i) (enhancement of the Hadley cell circulation) is not consistent with the observations because the change of winds was characterized by a daytime wind speed increase in the opposite direction that of the Hadley flow (see section 3). Hypothesis (ii) (dust modifies the atmospheric stability) would mostly result in a less stable atmosphere at night and, therefore, near-surface winds more coupled to the winds in the atmosphere aloft (Hess et al., 1977), which is not at all what is observed. However, this mechanism would also have the opposite effect during the day, and therefore, it would reduce the coupling between the near-surface slope flows (expected to be from the NE -ENE) and the winds aloft during daytime (expected to be from the NW), hence allowing the upslope anabatic winds to develop with

less competition from the synoptic flow, that is, resulting in the enhancement of the westward component of the wind vector. This scenario is similar to that observed right after the LDS decay (Figures 10d–10f), in that case due to the season approaching equinox and the consequent reduction in the Hadley cell strength (instead of the reduction in the coupling with such a flow present during the LDS onset). In any case, the result was similar: The westward component of the winds produced by the upslope anabatic winds during the midday and afternoon was enhanced, and a pronounced counterclockwise rotation was observed in the diurnal cycle. However, even with the weak Hadley cell circulation around the equinox described above, the resulting enhancement in the near-surface zonal component of wind observed by InSight (Figure 10e) was lower than that reached during the LDS onset (Figure 10b). Thus, even in the case that Hypothesis (ii) was enhancing the near-surface zonal winds during daytime and, therefore, explaining part of the observed effect, an additional force in opposition to the large-scale Hadley cell circulation would be needed to fully explain the observations.

On the other hand, Hypothesis (iii) (winds induced by the enhanced thermal tides) fits the observations, as the wind behavior changes occur when the pressure signature of the tides was at its maximum due to the asymmetry in the longitudinal dust loading, as discussed above. This is also supported by the LMD GCM numerical climate simulations performed under nominal dust conditions with a flattened topography around InSight (Figure SM4 in Banfield et al., 2020). In that simulation, where the effect of the slope winds has disappeared and in which only the dynamical effect of the thermal tides and occasional planetary waves can influence the diurnal cycle, it can be seen that the thermal tides induce changes in the wind direction between 6:00 and 18:00 LTST that are very consistent with the changes measured by InSight during the onset of the LDS. Thus, InSight observations and modeling suggest that enhanced tidal flows during the LDS onset, perhaps acting constructively with a reduced perturbation by the large-scale winds aloft, produced the strong easterly zonal component of the near-surface winds observed during the onset of the LDS (Figure 10b).

5. Convective Vortices

MSL's observations during the MY34 GDS demonstrated a complete cessation of imaged dust devils and inferred (from pressure data) convective vortices during the highly dusty phase of the GDS at MSL's location (Guzewich et al., 2019; Ordonez-Etxebarria, Hueso, & Sánchez-Lavega, 2020). According to the theory of Renno et al. (1998), which models convective vortices as heat engines, the number and/or strength of convective vortices depend on thermodynamic efficiency, which increases with increasing Planetary Boundary Layer (PBL) height, and on sensible heat flux, which mostly depends on near-surface wind speed and surface-to-air temperature differences (see also Newman, Kahanpää, et al., 2019). Thus, the strong reduction in surface insolation during the GDS ($\tau \sim 8.5$) led to a significant reduction in maximum surface-to-air temperatures reached during the daytime (see Figure 5 in Viúdez-Moreiras et al., 2019). The REMS WS was not operative during the GDS. However, given the origin of the local circulation that shapes the diurnal wind cycle, winds were probably reduced during the storm as suggested by modeling (Newman, Baker, et al., 2019). Also, as discussed in Spiga et al. (2020), wind can play a role by advecting vortices and making encounters with a stationary pressure sensor more frequent, such as those observed by the InSight lander. Hence, the combination of lower daytime surface-to-air temperature differences measured by REMS and the predicted lower winds could explain the decrease and cessation in the convective vortices observed by MSL during the highly dusty phase of the GDS.

Figure 11 shows the number of pressure drops observed for the first 200 sols of the mission (left column) and for the period encompassing onset of the LDS (right column) (see Banfield et al., 2020, and Spiga et al., 2020, for further details on the method to detect pressure drops). We show here the number of pressure drops, during the dust storm period, that were larger than 0.5 Pa (Figure 11, left) and 0.3 Pa (Figure 11, right). Other pressure drop intensity thresholds show similar evolutions. The observed variability of pressure drops during the LDS can be split into two periods. First, there was an enhancement during storm onset (Figure 11, right), which was consistent with the strong increase observed in the daytime wind speeds (~6 m/s prior to the LDS to ~11 m/s during the storm onset) within this period. The relatively weak reduction in surface-to-air thermal gradients (~45 K prior to the LDS to ~38 K during the opacity peak) during the MD timeslot which covers most of the dust devil activity, as a result of the increase in dust opacity within the LDS (τ peaks in Sol 52

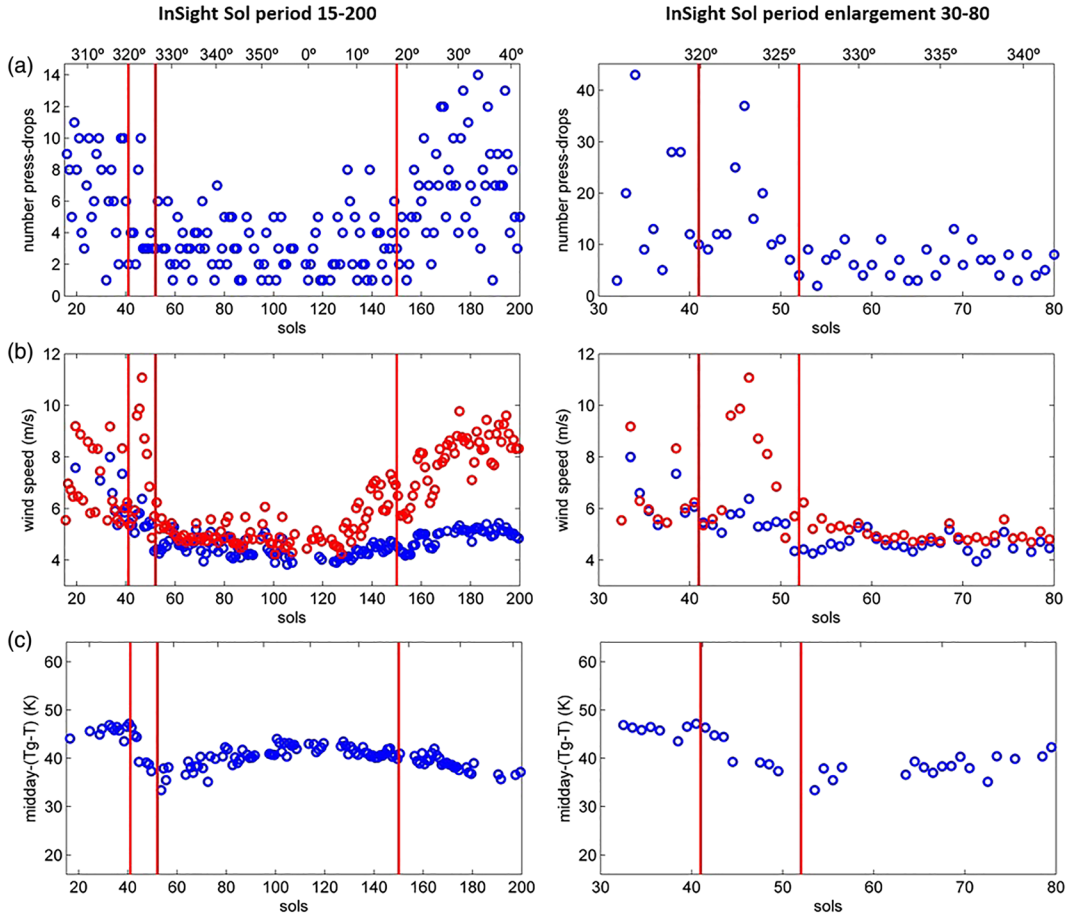


Figure 11. Number of pressure drops as a function of InSight sol and the relationship with surface-to-air thermal gradient and wind speed. (left column) Sol period 15–200 encompassing the full LDS. (right column) Sol period 30–80 encompassing LDS onset. (a) Number of pressure drops higher than 0.5 Pa (left) and 0.3 Pa (right), as shown in Spiga et al. (2020); (b) near-surface sol-average wind speed (blue color) and during the midday (10:00–15:00 LTST) timeslot (red color); and (c) difference between ground and air temperatures within the midday. Note that the latter may be biased due to the lander's thermal contamination of air temperature in particular. Vertical lines show the time of LDS onset (Sol 41), opacity peak (Sol 52), and end of decay stage (Sol 150).

to 1.9), was probably not enough to compensate for the effect of the increase in wind speeds during the onset of the LDS (see sections 4 and 5), resulting in the aforementioned enhancement in pressure drops. This differs from the observed effects during the highly dusty phase of the MY34 GDS, where much higher optical depths were reached, producing a much larger reduction in thermal gradients (Figure S4). Second, a pronounced decrease of vortex activity was then observed during the LDS decay (Sols 52–150), resulting from a strong decrease of wind speed. Wind patterns were not significantly perturbed *within this period* by the LDS (Figure 11 and see also sections 4 and 5), and only a relatively weak reduction in surface-to-air thermal gradients was observed (~10 K; Figure 11). Therefore, the near-surface wind patterns and thermal gradients response during the LDS decay, particularly since Sol ~60–70, mostly evolved in accordance to their seasonal behavior, and as a result, the observed evolution in pressure drops in Figure 11, associated with convective vortices, most likely follows its nominal seasonal evolution. It is difficult to differentiate between the effects of the LDS and the nominal seasonal evolution in the Sol Period 52–70, due to the lack of InSight data from previous MY. Additional observations during the mission will help to discern such effects (see Spiga et al., 2020, for further discussion on convective vortices). Note that InSight has not yet observed any dust devils in images (Banfield et al., 2020), despite larger vortex pressure drops being recorded than in Gale crater, which may be due to a lack of loftable dust, but this question remains unsolved to date.

6. Summary and Conclusions

NASA's InSight mission landed in Elysium Planitia (~4.5°N, 136°E) at Ls ~ 296°, right after the decay of the MY34 2018 GDS and before the onset of the MY34 2019 LDS. It was fortunate that the solar-powered InSight landed in atmospheric conditions without a dust storm, phenomena that to date remain unpredictable.

The MY34 2019 LDS was observed in detail by several orbiters and on the surface by MSL in Gale crater, which lies a similar distance from the equator (but to the south) and only ~600 km from InSight's landing site.

The LDS started in longitudes ~30–70°W, within the tropical region, in late December 2018 (MY34-L_s ~ 312°). MRO orbiter data showed a rapid growth of the storm to cover Chryse Planitia, Lunae Planum, Xanthe Terra, and Valles Marineris, with it reaching the locations of InSight and MSL at L_s ~ 320° (InSight Sol ~41). InSight's cameras observed increased optical depth, τ, during the LDS ranging from ~0.7 prior to onset to a peak of ~1.9 eleven Sols after (L_s ~ 326°). Given the sparse opacity measurements acquisition, the absolute peak in opacity may have been missed. Contemporaneous measurements by MSL showed similar values in Gale crater, with the opacity there reaching a peak of ~1.8. After that, the LDS decayed. Elevated levels of atmospheric dust persevered until the second half of March 2019, corresponding to the end of MY34 and recovering prestorm values for τ by mission Sol ~150. All atmospheric variables measured by InSight were significantly affected albeit at different times. The first effects were observed in pressure and wind patterns at Ls ~ 320°, corresponding to InSight mission Sol 41, which was confirmed in the IDC opacity measurements in Sol 48 (increase in τ from 0.843 ± 0.084 in mission Sol 38 to 1.292 ± 0.090 in Sol 48). The onset of the LDS was when the storm's impact on pressure and winds was the greatest, while air and ground temperatures disturbances evolved accordingly with τ, peaking at Sols 50–54 (Ls ~ 326°). These changes mostly reflect global and local responses, respectively, to the dust loading.

Pressure tides were strongly affected by the LDS. The diurnal pressure amplitude experienced an abrupt increase during onset of the LDS at InSight and MSL's locations, peaking on InSight Sol 45, and recovered their prestorm values with an oscillatory behavior a few sols later. The diurnal pressure mode's phase was also significantly disturbed during storm onset, being more disturbed at InSight's location. This enhancement of the diurnal mode amplitude was also observed in the tidal analysis of data during the two 1977 GDSs from the Viking Landers and in local and regional storms by MSL, in addition to the MY34 2018 GDS. The transitory amplitude and phase disturbances of the diurnal pressure mode observed during the 1977B GDS and 2018 GDS have been attributed to an enhancement of the nonmigrating Kelvin wave due to spatial asymmetries in the atmospheric dust abundance, which could also be influencing the observed behavior within the MY34 LDS onset. The semidiurnal pressure mode amplitude in both missions evolved, as expected, according to dust opacity, suggesting a high correspondence between the local opacity measured by both surface missions and the regional-to-global integrated atmospheric dust abundance, even during the LDS, and contrary to what was observed during the MY34 2018 in Gale crater, when local dust opacity measured by MSL peaked several sols before the global integrated atmospheric dust loading. The semidiurnal mode amplitude was higher at the MSL location, suggesting asymmetries in the latitudinal variation or a topographic effect, similarly to the previously reported effect in the diurnal pressure mode amplitude. The terdiurnal pressure mode amplitude was significantly enhanced during the onset of the LDS, which could be the result of hemispheric differences in atmospheric dust content during this period and nonlinear interactions between the diurnal and semidiurnal tides, and is compatible with the dust distribution observed by orbiters (Figure 3).

Minimum ground temperatures increased by ~5 K and peaked at Sol ~50, in accordance with the peak in opacity, as a consequence of the higher atmospheric dust load reducing the IR radiative cooling of the surface at night. On the other hand, maximum ground temperatures decreased by 9 K over the same period, as a result of the greater radiation absorption by the atmosphere during the daytime, which decreased the surface insolation.

The local air temperatures are strongly influenced by the lander's thermal effects and thus are thought to be quite different from the real atmospheric air temperature. The daytime perturbation strongly depends on wind speeds and directions. A simple preliminary air temperature retrieval based on that used by REMS strongly minimizes the lander's thermal contamination, particularly during the daytime. The retrieval strongly minimizes the observed overheating (~15–20 K) during the day and partially reduce the lander's

overcooling during the night (~10 K), although it does not remove it completely. The resulting nighttime atmospheric temperatures are ~5 K lower than surface temperatures at night, whereas theory and measurements made at other landing sites with similar surface properties (including those made by MSL) suggest that nighttime air temperatures should always be warmer than surface measurements. The similar values of both booms' nighttime temperatures, mostly independent of winds pattern, suggest that radiative heat transfer dominates during the night rather than the more influencing convective heat transfer during daytime, which is compatible with the very low surface-to-air thermal gradients (<10 K) at night in comparison with those reached during the day (~40 K) and low wind speeds. Therefore, it is difficult to interpret the evolution of the air temperature during the LDS. This variation is of the same order of magnitude as the sensor accuracy, lower than the lander's thermal perturbation, and overlaps with the expected nominal seasonal evolution of temperatures, which have not been characterized as yet. In any case, the estimated effect of the LDS on near-surface air temperatures is suggested to be weak (~5 K in the minimum temperatures, similarly to the ground temperatures, and ~3 K in the daily mean). However, the surface-to-air thermal gradients, peaking around midday, were reduced from ~45 K prior to the LDS to ~38 K during the opacity peak.

This is the first time since the Viking missions in the 1970s that a spacecraft with a fully functional WS has measured the effect of a regional dust storm. Winds were west-northwesterly in the daily mean at the beginning of the mission, as a result of the Hadley cell that dominated this season and whose flows were controlled by channeling effects of the regional topography at InSight's general location in Elysium Planitia. The interpretation of InSight's wind data is complicated by the interaction of the regional and local effects induced by topography with large-scale signatures such as the Hadley circulation and thermal tides, which impose a diurnal perturbation onto the mean wind, in family with observations by Viking landers data (Hess et al., 1977; Leovy & Zurek, 1979; Wilson & Hamilton, 1996). The diurnal wind pattern observed in northern winter is mainly attributed to regional and local effects induced by InSight's landing site slope rather than by thermal tides. Greater coupling was observed between surface winds and the winds aloft as the planetary boundary layer developed during the daytime. Winds during the LDS onset described a complete and marked counterclockwise rotation during each sol. However, the strong easterly winds during daytime suggest that an additional pressure force in opposition to the large-scale Hadley cell circulation is enhancing the zonal component of the near-surface winds during the onset of the LDS, which could be compatible with enhanced tidal flows in this period.

InSight observations suggest a variation in convective vortex abundance during the MY34 2019 LDS, with an overall decrease during the storm. However, the vortex activity remained strong during onset of the LDS due to the increase of wind speed and the relatively weak decrease in surface-to-air thermal gradient.

Observations in future MYs will help to differentiate the effects of the LDS from seasonal changes, assuming the same timing or magnitude of storm does not occur again.

Data Availability Statement

The data used in this work are available in the NASA's Planetary Data System (PDS) (https://pds.nasa.gov/). The wind and pressure data are obtained online (https://atmos.nmsu.edu/PDS/data/PDS4/InSight/). HP^3-RAD derived data are obtained online (https://pds-geosciences.wustl.edu/insight/urn-nasa-pds-insight_rad/). MSL data are obtained from https://atmos.nmsu.edu/data_and_services/atmospheres_data/MARS/curiosity/rems.html (MOD data set).

Acknowledgments

This research has been partially supported by the Spanish Ministry of Economy and Competiveness (MINECO), under Project ESP2016-79612-C3-1-R. French coauthors acknowledge support from Centre National d'Études Spatiales (CNES). C. E. N. acknowledges support from InSight Participating Scientist Grant 80NSSC18K1630. In addition, we wish to express our gratitude to the NASA's InSight and MSL missions for supporting this investigation. The authors thank Ricardo Hueso and an anonymous reviewer, whose comments helped improve this paper, and David Kass for his valuable comments on the evolution of the GDS based on the MCS orbital data. This paper is InSight Contribution 117.

References

Banfield, D., Rodriguez-Manfredi, J. A., Russell, C. T., Rowe, K. M., Leneman, D., Lai, H. R., et al. (2019). The InSight Auxiliary Payload Sensor Suite. *Space Science Reviews*, *215*(1), 4. https://doi.org/10.1007/s11214-018-0570-x

Banfield, D., Spiga, A., Newman, C., Forget, F., Lemmon, M., Lorenz, R., et al. (2020). The atmosphere of Mars as observed by InSight. *Nature Geoscience*, *13*(3), 190–198. https://doi.org/10.1038/s41561-020-0534-0

Basu, S., Wilson, J., Richardson, M., & Ingersoll, A. (2006). Simulation of spontaneous and variable global dust storms with the GFDL Mars GCM. *Journal of Geophysical Research*, *111*, E09004. https://doi.org/10.1029/2005JE002660

Cantor, B. A., James, P. B., Caplinger, M., & Wolff, M. J. (2001). Martian dust storms: 1999 Mars orbiter camera observations. *Journal of Geophysical Research*, *106*(E10), 23,653–23,687. https://doi.org/10.1029/2000JE001310

Chamberlain, T. E., Cole, H. L., Dutton, R. G., Greene, G. C., & Tillman, J. E. (1976). Atmospheric measurements on Mars: The Viking meteorology experiment. *Bulletin of the American Meteorological Society*, *57*(9), 1094–1104. https://doi.org/10.1175/1520-0477(1976)057<1094:amomtv>2.0.co;2

Domínguez, M., Jiménez, V., Ricart, J., Kowalski, L., Torres, J., Navarro, S., et al. (2008). A hot film anemometer for the Martian atmosphere. *Planetary and Space Science*, *56*(8), 1169–1179. https://doi.org/10.1016/j.pss.2008.02.013

Forget, F., Banfield, D., Millour, E., Spiga, A., Newman, C., Viúdez-Moreiras, D., et al. (2019). *Mars large scale meteorology observed by InSight*. Paper presented at EPSC-DPS Joint Meeting 2019, EPSC-DPS2019–903.

Gómez-Elvira, J., Armiens, C., Castañer, L., Domínguez, M., Genzer, M., Gómez, F., et al. (2012). REMS: The environmental sensor suite for the Mars Science Laboratory rover. *Space Science Reviews*, *170*(1–4), 583–640. https://doi.org/10.1007/s11214-012-9921-1

Guzewich, S. D., Lemmon, M., Smith, C. L., Martínez, G., Vicente-Retortillo, Á., Newman, C. E., et al. (2019). Mars Science Laboratory observations of the 2018/Mars year 34 global dust storm. *Geophysical Research Letters*, *46*, 71–79. https://doi.org/10.1029/2018GL080839

Guzewich, S. D., Newman, C. E., de la Torre Juarez, M., Wilson, R. J., Lemmon, M., Smith, M. D., et al. (2016). Atmospheric tides in Gale crater, Mars. *Icarus*, *268*, 37–49. https://doi.org/10.1016/j.icarus.2015.12.028

Heavens, N. G., McCleese, D. J., Richardson, M. I., Kass, D. M., Kleinböhl, A., & Schofield, J. T. (2011). Structure and dynamics of the Martian lower and middle atmosphere as observed by the Mars Climate Sounder: 2. Implications of the thermal structure and aerosol distributions for the mean meridional circulation. *Journal of Geophysical Research*, *116*, E01010. https://doi.org/10.1029/2010JE003713

Hess, S. L., Henry, R. M., Leovy, C. B., Ryan, J. A., & Tillman, J. E. (1977). Meteorological results from the surface of Mars: Viking 1 and 2. *Journal of Geophysical Research*, *82*(28), 4559–4574. https://doi.org/10.1029/JS082i028p04559

Jones, K. L., Arvidson, R. E., Guinness, E. A., Bragg, S. L., Wall, S. D., Carlston, C. E., & Pidek, D. G. (1979). One Mars year: Viking Lander imaging observations. *Science*, *204*(4395), 799–806. https://doi.org/10.1126/science.204.4395.799

Kass, D. M., Kleinböhl, A., McCleese, D. J., Schofield, J. T., & Smith, M. D. (2016). Interannual similarity in the Martian atmosphere during the dust storm season. *Geophysical Research Letters*, *43*, 6111–6118. https://doi.org/10.1002/2016GL068978

Kass, D. M., Schofield, J. T., Kleinböhl, A., McCleese, D. J., Heavens, N. G., Shirley, J. H., & Steele, L. J. (2019). Mars Climate Sounder observation of Mars' 2018 global dust storm. *Geophysical Research Letters*, *46*. https://doi.org/10.1029/2019GL083931

Kleinböhl, A., Wilson, R. J., Kass, D., Schofield, J. T., & McCleese, D. J. (2013). The semidiurnal tide in the middle atmosphere of Mars. *Geophysical Research Letters*, *40*, 1952–1959. https://doi.org/10.1002/grl.50497

Lemmon, M. T., Guzewich, S. D., McConnochie, T., Vicente-Retortillo, A., Martínez, G., Smith, M. D., et al. (2019). Large dust aerosol sizes seen during the 2018 Martian global dust event by the Curiosity rover. *Geophysical Research Letters*, *46*, 9448–9456. https://doi.org/10.1029/2019GL084407

Lemmon, M. T., Wolff, M. J., Bell, J. F. III, Smith, M. D., Cantor, B. A., & Smith, P. H. (2015). Dust aerosol, clouds, and the atmospheric optical depth record over 5 Mars years of the Mars Exploration Rover mission. *Icarus*, *251*, 96–111. https://doi.org/10.1016/j.icarus.2014.03.029

Leovy, C. B., & Zurek, R. W. (1979). Thermal tides and Martian dust storms: Direct evidence for coupling. *Journal of Geophysical Research*, *84*(B6), 2956–2968. https://doi.org/10.1029/JB084iB06p02956

Lewis, S. R., & Barker, P. R. (2005). Atmospheric tides in a Mars general circulation model with data assimilation. *Advances in Space Research*, *36*(11), 2162–2168. https://doi.org/10.1016/j.asr.2005.05.122

Maki, J. N., Golombek, M., Deen, R., Abarca, H., Sorice, C., Goodsall, T., et al. (2018). The color cameras on the InSight lander. *Space Science Reviews*, *214*(6), 105. https://doi.org/10.1007/s11214-018-0536-z

Malin, M. C., Cantor, B. A., Britton, A. W. (2018a). MRO MARCI Weather Report for the week of 10 December 2018–16 December 2018, Malin Space Science Systems Captioned Image Release, MSSS-560. http://www.msss.com/msss_images/2018/12/19/

Malin, M. C., Cantor, B. A., Britton, A. W. (2018b). MRO MARCI Weather Report for the week of 17 December 2018–23 December 2018, Malin Space Science Systems Captioned Image Release, MSSS-561. http://www.msss.com/msss_images/2018/12/26/

Malin, M. C., Cantor, B. A., Britton, A. W. (2018c). MRO MARCI Weather Report for the week of 24 December 2018–30 December 2018, Malin Space Science Systems Captioned Image Release, MSSS-562. http://www.msss.com/msss_images/2019/01/02/

Malin, M. C., Cantor, B. A., Britton, A. W. (2019). MRO MARCI Weather Report for the week of 21 January 2019–27 January 2019, Malin Space Science Systems Captioned Image Release, MSSS-563. http://www.msss.com/msss_images/2019/01/30/

Martínez, G. M., Newman, C. N., de Vicente-Retortillo, A., Fischer, E., Renno, N. O., Richardson, M. I., et al. (2017). The modern near-surface Martian climate: A review of in-situ meteorological data from Viking to Curiosity. *Space Science Reviews*, *212*(1-2), 295–338. https://doi.org/10.1007/s11214-017-0360-x

Montabone, L., Spiga, A., Kass, D. M., Kleinböhl, A., Forget, F., & Millour, E. (2020). Martian Year 34 column dust climatology from Mars Climate Sounder observations: Reconstructed maps and model simulations. *Journal of Geophysical Research: Planets*, *125*, e2019JE006111.

Morgan, P., Grott, M., Knapmeyer-Endrun, B., Golombek, M., Delage, P., Lognonné, P., et al. (2018). A pre-landing assessment of regolith properties at the InSight landing site. *Space Science Reviews*, *214*(6), 104. https://doi.org/10.1007/s11214-018-0537-y

Mueller, D. W., & Abu-Mulaweh, H. I. (2006). Prediction of the temperature in a fin cooled by natural convection and radiation. *Applied Thermal Engineering*, *26*, 1662–1668.

Mueller, N. T., Knollenberg, J., Grott, M., Kopp, E., Walter, I., Krause, C., et al. (2020). Calibration of the HP^3 radiometer on InSight. *Earth and Space Science*, *7*, e2020EA001086. https://doi.org/10.1029/2020EA001086

Newman, C., Baker, M., Banfield, D., de la Torre, M., Forget, F., Gómez-Elvira, J., et al. (2019). *The impact of dust storms on the near-surface meteorology of Mars*. Paper presented at EPSC-DPS Joint Meeting 2019, Geneva, Switzerland.

Newman, C. E., Gómez-Elvira, J., Marín, M., Navarro, S., Torres, J., Richardson, M. I., et al. (2017). Winds measured by the Rover Environmental Monitoring Station (REMS) during the Mars Science Laboratory (MSL) rover's Bagnold Dunes Campaign and comparison with numerical modeling using MarsWRF. *Icarus*, *291*, 203–231. https://doi.org/10.1016/j.icarus.2016.12.016

Newman, C. E., Kahanpää, H., Richardson, M. I., Martínez, G. M., Vicente-Retortillo, A., & Lemmon, M. T. (2019). MarsWRF convective vortex and dust devil predictions for Gale Crater over 3 Mars years and comparison with MSL-REMS observations. *Journal of Geophysical Research: Planets*, *124*(12), 3442–3468. https://doi.org/10.1029/2019JE006082

Ordonez-Etxeberria, I., Hueso, R., & Sánchez-Lavega, A. (2020). Strong increase in dust devil activity at Gale crater on the third year of the MSL mission and suppresion during the 2018 Global Dust Storm. *Icarus*, *347*, 113814. https://doi.org/10.1016/j.icarus.2020.113814

Ordóñez-Etxeberría, I., Hueso, R., Sánchez-Lavega, A., Millour, E., & Forget, F. (2019). Meteorological pressure at Gale crater from a comparison of REMS/MSL data and MCD modelling: Effect of dust storms. *Icarus*, *317*, 591–609. https://doi.org/10.1016/j.icarus.2018.09.003

Ordonez-Etxeberria, I., Hueso, R., Sánchez-Lavega, A., & Vicente-Retortillo, Á. (2020). Characterization of a local dust storm on Mars with REMS/MSL measurements and MARCI/MRO images. *Icarus*, *338*, 113521. https://doi.org/10.1016/j.icarus.2019.113521

Rafkin, S. C. R. (2009). A positive radiative-dynamic feedback mechanism for the maintenance and growth of Martian dust storms. *Journal of Geophysical Research*, *114*, E01009. https://doi.org/10.1029/2008JE003217

Renno, N. O., Burkett, M., & Larkin, M. P. (1998). A simple thermodynamical theory for dust devils. *Journal of the Atmospheric Sciences*, *55*(21), 3244–3252. https://doi.org/10.1175/1520-0469(1998)055<3244:ASTTFD>2.0.CO;2

Richardson, M. I., & Newman, C. E. (2018). On the relationship between surface pressure, terrain elevation, and air temperature. Part I: The large diurnal surface pressure range at Gale crater, Mars and its origin due to lateral hydrostatic adjustment. *Planetary and Space Science*, *164*, 132–157. https://doi.org/10.1016/j.pss.2018.07.003

Ryan, J. A., & Henry, R. M. (1979). Mars atmospheric phenomena during major dust storms, as measured at surface. *Journal of Geophysical Research*, *84*(B6), 2821–2829. https://doi.org/10.1029/JB084iB06p02821

Ryan, J. A., & Sharmann, R. M. (1981). Two major dust storms, one Mars year apart: Comparison from Viking data. *Journal of Geophysical Research*, *86*(C4), 3247–3254. https://doi.org/10.1029/JC086iC04p03247

Sánchez-Lavega, A., del Río-Gaztelurrutia, T., Hernández-Bernal, J., & Delcroix, M. (2019). The onset and growth of the 2018 Martian global dust storm. *Geophysical Research Letters*, *46*, 6101–6108. https://doi.org/10.1029/2019GL083207

Savijärvi, H., Martinez, G., Harri, A. M., & Paton, M. (2020). Curiosity observations and column model integrations for a Martian global dust event. *Icarus*, *337*, 113515. https://doi.org/10.1016/j.icarus.2019.113515

Smith, A. K., & Ortland, D. A. (2001). Modeling and analysis of the structure and generation of the terdiurnal tide. *Journal of the Atmospheric Sciences*, *58*(21), 3116–3134. https://doi.org/10.1175/1520-0469(2001)058<3116:maaots>2.0.co;2

Smith, M. D. (2019). THEMIS observations of the 2018 Mars global dust storm. *Journal of Geophysical Research: Planets*, *124*(11), 2929–2944. https://doi.org/10.1029/2019JE006107

Spiga, A., Banfield, D., Teanby, N. A., Forget, F., Lucas, A., Kenda, B., et al. (2018). Atmospheric science with InSight. *Space Science Reviews*, *214*, 109. https://doi.org/10.1007/s11214-018-0543-0

Spiga, A., Murdoch, N., Lorenz, R., Forget, F., Newman, C., Rodriguez, S., et al. (2020). A study of daytime convective vortices and cells in the Martian Planetary Boundary Layer after half a year of InSight measurements and comparisons with large-eddy simulations. *Journal of Geophysical Research*, this issue (under review). https://ui.adsabs.harvard.edu/abs/2020arXiv200501134S/abstract

Spohn, T., Grott, M., Smrekar, S. E., Knollenberg, J., Hudson, T. L., Krause, C., et al. (2018). The Heat Flow and Physical Properties Package (HP^3) for the InSight Mission. *Space Science Reviews*, *214*(5), 96. https://doi.org/10.1007/s11214-018-0531-4

Stamnes, K., Tsay, S.-C., Wiscombe, W., & Jayaweera, K. (1988). Numerically stable algorithm for discrete-ordinate-method radiative transfer in multiple scattering and emitting layered media. *Applied Optics*, *27*(12), 2502. https://doi.org/10.1364/AO.27.002502

Teitelbaum, H., Vial, F., Manson, A. H., Giraldez, R., & Massebeuf, M. (1989). Non-linear interaction between the diurnal and semidiurnal tides: Terdiurnal and diurnal secondary waves. *Journal of Atmospheric and Terrestrial Physics*, *51*(7-8), 627–634. https://doi.org/10.1016/0021-9169(89)90061-5

Tillman, J. E. (1984). In C. P. McKay (Ed.), *Martian meteorology and dust storms from Viking observations* (Vol. 62, pp. 333–342). Paper presented at Proceedings of the Case for Mars II Conference, Boulder CO.

Tillman, J. E. (1988). Mars global atmospheric oscillations: Annually syncronized, transient normal-mode oscillations and the triggering of global dust storms. *Journal of Geophysical Research*, *93*(D8), 9433–9451. https://doi.org/10.1029/JD093iD08p09433

Viúdez-Moreiras, D., Gómez-Elvira, J., Newman, C. E., Navarro, S., Marin, M., Torres, J., de la Torre, M., & MSL Team (2019a). Gale surface wind characterization based on the Mars Science Laboratory REMS dataset. Part I: Wind retrieval and Gale's wind speeds and directions. *Icarus*, *319*, 909–925.

Viúdez-Moreiras, D., Gómez-Elvira, J., Newman, C. E., Navarro, S., Marin, M., Torres, J., de la Torre, M., & MSL Team (2019b). Gale surface wind characterization based on the Mars Science Laboratory REMS dataset. Part II: Wind Probability Distributions. *Icarus*, *319*, 645–656.

Viúdez-Moreiras, D., Newman, C. E., de la Torre, M., Martinez, G., Guzewich, S., Lemmon, M., et al. (2019). Effects of the MY34/2018 Global Dust Storm as measured by MSL REMS in Gale crater. *Journal of Geophysical Research: Planets*, *124*, 1899–1912. https://doi.org/10.1029/2019JE005985

Wang, H., & Richardson, M. I. (2015). The origin, evolution, and trajectory of large dust storms on Mars during Mars years 24-30 (1999-2011). *Icarus*, *251*, 112–127. https://doi.org/10.1016/j.icarus.2013.10.033

Wilson, R. J., & Hamilton, K. P. (1996). Comprehensive model simulation of thermal tides in the Martian atmosphere. *Journal of the Atmospheric Sciences*, *53*(9), 1290–1326. https://doi.org/10.1175/1520-0469(1996)053<1290:CMSOTT>2.0.CO;2

Wilson, R. J., & Richardson, M. I. (2000). The Martian atmosphere during the Viking mission, I: Infrared measurements of atmospheric temperatures revisited. *Icarus*, *145*(2), 555–579. https://doi.org/10.1006/icar.2000.6378

Zurek, R. W. (1976). Diurnal tide in the Martian atmosphere. *Journal of the Atmospheric Sciences*, *33*(2), 321–337. https://doi.org/10.1175/1520-0469(1976)033<0321:DTITMA>2.0.CO;2

Zurek, R. W., & Leovy, C. B. (1981). Thermal tides in the dusty Martian atmosphere: A verification of theory. *Science*, *213*, 437–439.

Zurek, R. W., & Martin, L. J. (1993). Interannual variability of planet-encircling dust storms on Mars. *Journal of Geophysical Research*, *98*(E2), 3247–3259. https://doi.org/10.1029/92JE02936